iGABASnFR2: Improved genetically encoded protein sensors of GABA

Ilya Kolb[1,2]*, Jeremy P. Hasseman[1,2]*, Akihiro Matsumoto[3,4], Thomas P. Jensen[5], Olga Kopach[5,6], Benjamin J. Arthur[1], Yan Zhang[1,7], Arthur Tsang[1,2], Daniel Reep[1,2], Getahun Tsegaye[1,2], Jihong Zheng[1,2], Ronak H. Patel[1,7], Loren L. Looger[8], Jonathan S. Marvin[1,7], Wyatt L. Korff[1,2], Dmitri A. Rusakov[5], Keisuke Yonehara[3,4], GENIE Project Team, Glenn C. Turner[1,2†]

* Equal contribution

† Correspondence: turnerg@janelia.hhmi.org

Affiliations

1. Janelia Research Campus, Howard Hughes Medical Institute, Ashburn, Virginia, USA
2. Janelia GENIE Project Team, Janelia Research Campus, Howard Hughes Medical Institute, Ashburn, Virginia, USA
3. Department of Gene Function and Phenomics, National Institute of Genetics, Mishima, Japan.
4. Graduate Institute for Advanced Studies, SOKENDAI, Hayama, Japan.
5. UCL Queen Square Institute of Neurology, University College London, Queen Square, London WC1N 3BG, U.K.
6. Neuroscience and Cell Biology Research Institute, City St George's University of London, Cranmer Terrace, London SW17 0RE, UK
7. Janelia Tool Translation Team, Janelia Research Campus, Howard Hughes Medical Institute, Ashburn, Virginia, USA
8. HHMI, Department of Neurosciences, University of California, San Diego, La Jolla, California, USA

Abstract

Monitoring GABAergic inhibition in the nervous system has been enabled by development of an intensiometric molecular sensor that directly detects GABA. However, the first generation iGABASnFR exhibits low signal-to-noise and suboptimal kinetics, making in vivo experiments challenging. To improve sensor performance, we targeted several sites in the protein for near-saturation mutagenesis and evaluated the resulting sensor variants in a high throughput screening system using evoked synaptic release in primary cultured neurons. This identified a sensor variant, iGABASnFR2, with 4.2-fold improved sensitivity and 20% faster kinetics, and binding affinity that remained in a range sensitive to changes in GABA concentration at synapses. We also identified sensors with an inverted response, decreasing fluorescence intensity upon GABA binding. We termed the best such negative-going sensor iGABASnFR2n, which can be used to corroborate observations with the positive-going sensor. These improvements yielded a qualitative enhancement of in vivo performance when compared directly to the original sensor. iGABASnFR2 enabled the first measurements of direction-selective GABA release in the retina. In vivo imaging in somatosensory cortex revealed that iGABASnFR2 can report volume-transmitted GABA release following whisker stimulation. Overall, the improved sensitivity and kinetics of iGABASnFR2 make it a more effective tool for imaging GABAergic transmission in intact neural circuits.

Introduction

Genetically encoded neurotransmitter sensors have significantly advanced neuroscience by enabling direct, real-time monitoring of neurotransmitter dynamics. These tools have facilitated the study of synaptic transmission, input-output relationships within individual neurons, and large-scale network activity. Among these, genetically encoded sensors for GABA are particularly desirable due to the inherent challenges of detecting inhibitory signaling. GABAergic neurotransmission plays a crucial role in shaping neural circuit dynamics and maintaining the balance between excitation and inhibition across the brain. Disruptions in GABAergic signaling have been implicated in neurological and psychiatric disorders, including epilepsy, schizophrenia, and autism, highlighting the importance of developing sensitive tools to study inhibitory transmission (Sohal & Rubenstein 2019).

Although there are other techniques to measure GABA levels in the brain, they are limited in their sensitivity and/or spatiotemporal resolution. Microdialysis allows direct, quantitative measurement of extracellular GABA, even in human patients, but its temporal resolution is restricted to the scale of minutes (van der Zeyden et al. 2008). Electrophysiological approaches, while offering high sensitivity and temporal precision, do not scale to large neuronal populations and cannot independently distinguish GABAergic signaling from other hyperpolarizing currents (Macdonald & Olsen 1994). These limitations underscore the need for improved genetically encoded fluorescent sensors capable of resolving GABA dynamics with greater sensitivity, specificity, and temporal resolution.

We previously developed an intensity-based GABA Sensing Fluorescent Reporter, iGABASnFR, that increases fluorescence in the presence of GABA (Marvin et al. 2019), from here on referred to as iGABASnFR1. Like many sensors (Marvin et al. 2011), this design used a periplasmic binding protein from bacteria as the ligand binding domain, in this case Pf622 from the bacterium *Pseudomonas fluorescens*. A circularly permuted superfolder GFP (cpSFGFP) was then inserted at a site that supports fluorescence changes associated with GABA binding, and the protein was given trafficking sequences to localize it to the membrane. While this sensor enabled optical monitoring of GABAergic activity, its sensitivity and dynamic range remained limited compared to extensively optimized sensors like jGCaMP and iGluSnFR (Zhang et al. 2023; Aggarwal et al. 2023). In neuronal culture, the original iGABASnFR1 exhibited a half-maximal effective concentration (EC_{50}) of ~30 μM and maximal ΔF/F of ~0.6. A binding pocket mutation (F102G) increased the maximal ΔF/F of the sensor but at the cost of an increased EC_{50} and poor membrane localization. As such, the overall performance of iGABASnFR1 was not well-suited for high-resolution, photon-limited imaging applications.

To address these limitations, we used site-directed mutagenesis to engineer two next-generation GABA sensors, iGABASnFR2 and iGABASnFR2n. These sensors exhibit improved sensitivities and affinities for GABA, with positive- and negative-going fluorescence responses, respectively. Here, we describe the development and characterization of these enhanced GABA sensors and demonstrate their application in imaging inhibitory neurotransmission.

Results

Screening for improved variants

The original iGABASnFR1 (Fig. 1a, top) was engineered to increase fluorescence in the presence of GABA, and express robustly in mammalian neurons, making it a valuable addition to the suite of biosensors available to study the brain (Marvin et al. 2019; Looger & Griesbeck 2012; Dong et al. 2022; Yang et al. 2024). However, iGABASnFR1 is a first-generation sensor, with low sensitivity in vivo, particularly in comparison to other sensors such as jGCaMP and iGluSnFR, which have been subjected to multiple generations of engineering. Consequently, we applied the same screening pipeline used to optimize jGCaMP (Wardill et al. 2013; Zhang et al. 2023; Dana et al. 2016) to the task of improving iGABASnFR performance. This pipeline uses field stimulation to evoke activity of cultured primary neurons expressing different sensor variants. Stimulation elicits synaptic release, allowing us to screen for improved sensor performance by measuring response amplitude and kinetics (Fig. 1b), in an experimental setting that approximates in vivo conditions.

Sensor variants were derived by near-saturation mutagenesis of selected sites within the protein, and performance evaluated in a first round of screening. To select improved variants, we jointly optimized for both the ΔF/F of the sensor and its expression levels. Screening for expression was necessary because in our previous effort to engineer iGABASnFR (Marvin et al. 2019), we discovered several mutations, most notably, F102G, that increased the maximal ΔF/F but exhibited expression problems in neurons, with low baseline fluorescence and intracellular aggregates. We quantified the expression levels of different variants by counting the total number of pixels in a well that showed a significant increase in fluorescence during the field stimulation period. These pixels were classified as responsive pixels.

To guide our site-selection efforts, we used the unliganded crystal structure of a preliminary version of iGABASnFR https://www.rcsb.org/structure/6dgv (Marvin et al. 2019), a strategy that worked well for optimizing GCaMP (Akerboom et al. 2009). Specifically, we identified 39 sites to target: 14 near the GABA binding site, 6 at or around the protein hinge area, 10 on the cpSFGFP and 9 at the interface between the two ligand-binding and cpGFP domains (Fig. 1a, bottom).

In the first round of screening, these 39 sites were targeted for mutagenesis, generating 9±5 substitutions at each site (range: 1 to 19) for a total of 3947 variants. Sensor variants were arrayed in 96-well plates, with each plate containing 4 replicate wells of the same variant, and 8 replicate wells of the original iGABASnFR, which served as part of our quality control measures. Each well received 1, 10 and 40 field stimulation pulses separated by 12 ms, and we calculated responses by averaging fluorescence changes over all the responsive pixels in each well. We found 93 mutants with ΔF/F significantly higher than in-plate iGABASnFR1 controls and 22 of those also had a higher fraction of responsive pixels than iGABASnFR, indicating improved expression (Fig. 1c). Interestingly, at least 20 sequence-confirmed mutations, located in 5 different positions - $R168_{Pf}$, $D276_{Pf}$, $T203_{gfp}$, $V150_{gfp}$ and $V272_{Pf}$ - inverted the response of the sensor, making it decrease in fluorescence with field stimulation (number refers to location in the protein domain denoted by subscript, either cpSFGFP or the ligand binding Pf622). However, none of the inverted sensors exhibited |ΔF/F| greater than that of iGABASnFR. Among them, the

$R168_{gfp}P$ mutant was the most promising, with relatively high ΔF/F (0.6x of iGABASnFR) and expression (2x responsive pixels of iGABASnFR; Fig. 1c).

Although we found many marginally improved variants in the first round of screening, there was no clear winner that could be considered to be a major improvement over iGABASnFR. The most sensitive positive-going mutant in the screen was the previously known mutation $F102_{Pf}G$ (ΔF/F 2.5x of iGABASnFR) which was confirmed to have poor expression (0.3x responsive pixels of iGABASnFR). Similarly, the top-expressing mutant in the screen ($L178_{gfp}Y$; 14.8x responsive pixels of iGABASnFR) had only a modest ΔF/F (1.1x of iGABASnFR). Therefore, in the first round of screening, we succeeded in improving ΔF/F and expression separately but not jointly.

Enhancing performance with combinations of single site mutants

We hypothesized that we could generate variants with both improved sensitivity and expression by combining mutations that conveyed each property separately. To test this, the mutations $S99_{Pf}$→A/G/C, $F102_{Pf}$→G/Y, $F104_{Pf}$→Y/H, $R168_{gfp}$→P, $L178_{gfp}$→R/S, and $K253_{Pf}$→I/Y (labeled in Fig. 1d as plus signs) were chosen based on their performance in the first round and combined to create 635 double mutants, which were then screened in a second round. A large percentage of these mutants (49%) did not pass quality control to be considered for further analysis. The majority of these mutants had poor expression, no detectable response to field stimulation, or both. Of the remaining mutants, 52 exhibited improved expression and ΔF/F over iGABASnFR. More importantly, 27 mutants exhibited ΔF/F higher than $F102_{Pf}G$ and expression better than iGABASnFR, suggesting that our hypothesis was correct and the beneficial properties of the mutants could be additive. Interestingly, many of the mutations that improved ΔF/F and expression in positive-going sensors, did the same in negative-going sensors.

Of these variants, the best combination of dynamic range and expression was the mutant iGABASnFR.$S99_{Pf}A$.$F102_{Pf}Y$.$F104_{Pf}Y$.$L178_{gfp}S$, (hereafter iGABASnFR2). The best variant with inverted signal, iGABASnFR.$S99_{Pf}A$.$F104_{Pf}H$.$R168_{gfp}P$ was designated iGABASnFR2n (for negative-going). When we quantified rise time, peak ΔF/F and signal-to-noise, iGABASnFR2 performance was broadly superior to the original across all field stimulation conditions (Figure 2). For 10 action potentials (APs), iGABASnFR2 exhibited a peak ΔF/F 4.2-fold greater than iGABASnFR1 (iGABASnFR2 0.80 ± 0.12; iGABASnFR1 0.19 ± 0.02; p = 6.41e-28 Tukey's HSD post hoc test following one-way ANOVA), and a signal-to-noise ratio (SNR) 3-fold higher (iGABASnFR2 70.5 ± 10.7; iGABASnFR1 23.6 ± 5.7; p = 6.37e-23). Rise times were slightly faster (iGABASnFR2 38 ± 10 ms; iGABASnFR1 47 ± 21 ms; p = 0.13). The negative-going iGABASnFR2n exhibited slightly reduced performance relative to iGABASnFR2, but still achieved a 3.2-fold greater peak ΔF/F (iGABASnFR2n 0.61 ± 0.12; iGABASnFR1 0.19 ± 0.02; p = 2.50e-19), and 30% higher SNR compared to iGABASnFR1 (iGABASnFR2n 30.2 ± 10.0; iGABASnFR1 23.6 ± 5.7; p = 0.06). However, its kinetics were slower, with a rise time of 71 ± 10 ms. These measures clearly indicate that this next generation of GABASnFRs exhibit broadly improved performance in detecting GABA dynamics during synaptic release.

Structure of the iGABASnFR2-GABA complex

To gain some insight into the structure-function relationship of this sensor, we solved the crystal structure of iGABASnFR2 in complex with GABA (Fig. 3). To examine the conformational changes that accompany GABA binding, we compared this new liganded structure with the apo-form of a precursor of the original iGABASnFR (PDB ID 6DGV). Superimposing the structures, using cpGFP as a reference, revealed that the two lobes of the Venus flytrap domain in Pf622 shift closer together to secure GABA in the binding pocket (Fig. 3a). This conformational change resembles those seen in other bacterial periplasmic amino acid-binding proteins (Quiocho & Ledvina 1996).

The hinge region of Pf622, which connects the two lobes, likely plays a key role in allosteric modulation of ligand binding (Telmer & Shilton 2003; Marvin & Hellinga 2001); (Marvin et al. 2019; Planamente et al. 2012; Planamente et al. 2010). Within that hinge region, the F101L mutation, introduced in the original iGABASnFR1 (Marvin et al. 2019), increased binding affinity 10-fold (Fig. 3b). Also in the hinge region, residue S99 forms hydrogen bonds with the OD2 atom of D59 and NE2 atom of Q17, while the S99A mutation in iGABASnFR2 abolishes these interactions, potentially making the hinge region more flexible.

The GABA binding site itself is defined by the side chains of W9, T13, F100, Y102, W202, R205, D228, and Y264 (Fig. 3c). In iGABASnFR2, two mutations near the ligand binding site enhance interactions: F102Y forms a hydrogen bond via its hydroxyl group with D228, which, in turn, makes a hydrogen bond with the GABA amino group. And F104Y, while farther from the binding site, helps position W202 to interact with GABA through van der Waals forces. These likely contribute to the increased affinity for GABA we describe below.

Mutations at the interface between the ligand-binding domain and cpGFP modulate ligand-binding-induced fluorescence changes in many sensors (Akerboom et al. 2009; Zhang et al. 2023; Ding et al. 2014). In iGABASnFR2, the $L178_{gfp}S$ mutation at this interface is likely involved in a hydrogen-bonding network with nearby hydrophilic residues, enhancing the GABA-induced fluorescence change (Supplementary Fig. 1B). The N260A mutation in iGABASnFR1 eliminates side chain hydrogen bonding, removes a cryptic N-linked glycosylation site (N-X-S/T), and enhances protein expression. Another critical mutation, $F145_{gfp}W$, introduced in the original iGABASnFR1 to improve ΔF/F0, interacts directly with the hydroxyl group in the chromophore and surrounding residues.

Interestingly, although the Venus flytrap domain undergoes significant conformational changes upon GABA binding, cpGFP and its flanking linkers (along with up to four adjacent residues) do not show notable conformational changes (Fig. 3a). The structural difference between the unliganded and liganded forms shows a root mean square deviation of only 0.25 Å. This finding contrasts with observations in GCaMP (Zhang et al. 2023; Akerboom et al. 2009; Akerboom et al. 2012), where calcium binding to calmodulin induces substantial conformational changes at the interface, contributing to the large change in fluorescence with this sensor. These differences suggest a potential strategy to further enhance the performance of iGABASnFR2.

Biochemical Characterization

For *in vivo* applications, the effectiveness of the sensor depends on both its affinity for GABA, as well as the kinetics of GABA binding. Sensor affinity should not be so high that it is saturated by tonic levels of GABA in the brain, but should of course be in a range sensitive to the changes in concentration achieved during synaptic release. In mammals, extrasynaptic GABA concentrations lie in the low micromolar range (0.2–2.5 μM (Roth & Draguhn 2012; Glykys & Mody 2007; Lerma et al. 1986; Tossman et al. 1986), while synaptically released GABA can transiently reach low millimolar concentrations (~1.5–3 mM (Roth & Draguhn 2012; Mozrzymas et al. 2003; Barberis et al. 2004). The half-maximal effective concentration (EC_{50}) of iGABASnFR1 when it is expressed on the surface of neurons is 30 μM, so increasing sensor affinity could potentially lead to improved performance *in vivo* without contaminating signal from tonic GABA levels. However, kinetics are also important - the rapid changes in GABA concentration during synaptic release mean that sensor kinetics have to be fast enough to detect the change before GABA concentrations drop back down due to re-uptake and diffusion.

We first determined sensor affinities by titrating GABA concentration while monitoring fluorescence of purified protein. Somewhat surprisingly, purified iGABASnFR2 showed a smaller dynamic range than iGABASnFR1, although its affinity was higher (Fig. 4a; max dF/F0 iGABASnFR2: 0.45, iGABASnFR1: 1.82; EC_{50} iGABASnFR2 = 1.1 μM, iGABASnFR1 = 5.7 μM). It also displayed high selectivity for GABA over structurally related compounds (Fig. 4 – figure supplement 1), none of which interfered with GABA binding (Fig. 4 – figure supplement 2). Previous work with iGluSnFR showed that titrations with purified protein can exhibit different affinity values than when expressed on the membrane of cultured neurons (Aggarwal et al. 2023). The origins of this discrepancy are not clear, however on-cell titrations are closer to the operating environment of the sensor and are likely the more accurate predictor of *in vivo* performance. We found that on cells the half-maximal effective concentration (EC_{50}) of iGABASnFR2 was 6.4 ± 0.21 μM, a 7-fold higher affinity than iGABASnFR1 and 22-fold higher than iGABASnFR.F102$_{Pf}$G (Fig. 4b). So the improved performance we observed likely stems, in part, from this increased on-cell affinity, which nevertheless remains above background levels of GABA measured in the mammalian brain.

We examined sensor kinetics to step changes in GABA concentration using stopped-flow measurements. Relative to iGABASnFR1, the observed reaction rate constants were far greater for both iGABASnFR2 and iGABASnFR2n (Fig. 4c). iGABASnFR1 exhibits biphasic kinetics, with a relatively fast initial change compounded with a much longer phase before sensor saturation is reached (Marvin et al. 2019). In contrast, both iGABASnFR2 and iGABASnFR2n kinetics were accurately captured by fitting with a single exponential function, indicating a less complex relationship between ligand binding and changes in fluorescence (Fig. 4d). Although significantly faster than the first version, the kinetics of iGABASnFR2 and 2n are still slower than iGluSnFR3 (Aggarwal et al. 2023), suggesting further improvements in sensor performance would be possible if kinetics could be accelerated.

The 1p and 2p spectra of all sensors were similar (Fig 4e,f), as were their apparent pKa values (Fig. 4 - fig. supp. 3); additional biophysical properties are reported in Table 1. Overall, both kinetic and thermodynamic observations suggest that iGABASnFR2 and 2n offer a major

245 improvement in sensing GABA over the previously available sensor. We next tested this by
246 evaluating performance in vivo.

247 **Evaluating Sensor Performance in Intact Retina**

248 To evaluate indicator performance in an intact neural circuit, we examined synaptic transmission
249 in the retina. GABAergic inhibition is believed to play a pivotal role in generating direction-
250 selective responses to motion in the retina (Briggman et al. 2011; Yonehara et al. 2011).
251 Direction-selectivity is thought to originate in starburst amacrine cells (SACs), which extend
252 radially symmetric dendrites from a centrally located soma. Inputs to SACs are sprinkled across
253 the entire dendritic arbor, while the outputs are confined to varicosities located near the dendritic
254 tips.

255 Motion-selectivity is proposed to arise from differential GABA release. Specifically, the hypothesis
256 is that GABA release is stronger when a visual stimulus moves so that excitation sweeps down
257 the dendritic branch from root to tip (centrifugal motion) rather than when it sweeps from tip to
258 root (centripetal motion) (Fig. 5a). The resulting direction-selective inhibition is relayed to
259 direction-selective retinal ganglion cells (DSGCs) through asymmetric synaptic connections
260 (Briggman et al. 2011; Yonehara et al. 2011) (Fig. 5b). By inhibiting DSGC responses to motion
261 in the null direction, SAC inputs ensure that DSGC output is highly selective for motion in the
262 preferred direction, which is subsequently transmitted to the brain.

263 Notably, the evidence for this centrifugal selectivity has been obtained by electrophysiological
264 membrane potential recording and two-photon Ca^{2+} imaging from starburst cells (Euler et al. 2002;
265 Vaney et al. 2012). Direct evidence for direction-selective GABA release has been lacking, and
266 imaging GABA release from the starburst cell dendrites would provide important confirmation of
267 the origin of retinal direction selectivity.

268 We virally transfected starburst amacrine cells with iGABASnFR1 or iGABASnFR2, using a Cre-
269 Lox system for cellular specificity. 6-8 weeks after injection, we dissected retinae and performed
270 two-photon imaging, analyzing activity within small fields of view expected to contain multiple
271 release sites on the amacrine cell dendrites.

272 We first tested whether we could detect responses to light flashes with a 500 μm spot that covered
273 the entire field of view. iGABASnFR1 showed weak but measurable signals to this full-field
274 stimulation, although detecting responses on single trials was challenging. However, when
275 presented with moving dots, the weak signal made it very difficult to detect direction selectivity,
276 even after trial-averaging. By contrast, iGABASnFR2 responses to static flashes were large
277 enough to be detected on single trials, and robust direction-selectivity of GABA release was
278 readily observed in response to motion stimuli.

279 We quantified the quality of the signals by computing two measures: 1) response amplitude index
280 (RAI), which denotes the light-evoked response strength and 2) response reliability, which reflects
281 trial-to-trial variance (Methods) (Baden et al. 2016). Overall, both the response amplitudes and
282 the reliability of the responses were significantly higher with iGABASnFR2 than with iGABASnFR1
283 (Fig. 5i,j). In particular, response reliability was much improved in iGABASnFR2 (mean ± SD
284 iGABASnFR2: 0.66 ± 0.14; iGABASnFR: 0.41 ± 0.11), indicating that this sensor reveals activity
285 that previously would have been below detection threshold.

286 We also examined the signal-to-noise ratio (SNR) of the responses to motion, comparing
287 response amplitude to the variance of signals at baseline. Compared with iGABASnFR1 signals,
288 iGABASnFR2 signals had significantly higher SNR with both larger signals and lower variance of
289 the baseline (Fig. 5k,l). The improved SNR and higher response reliability across trials resulted
290 in stable motion responses with lower circular variance (CV; Fig. 5m), yielding better direction
291 selectivity measurements overall. Overall, the improved performance of iGABASnFR2 not only
292 enabled us to detect more responses but also provided a more accurate measure of GABA
293 release evoked by visual motion, directly demonstrating that starburst cells release GABA in a
294 direction-selective manner.

295 **Sensor Performance at Individual Cell Axons and in vivo**

296 As a first step toward in vivo application, we tested whether iGABASnFR could detect GABA
297 release from single interneuron activation in brain slices. We expressed either iGABASnFR1 or
298 iGABASnFR2 in hippocampal neurons, using viral delivery in mice to obtain acute slices (viral
299 titre 0.1E10), or by biolistic transfection in organotypic hippocampal slice cultures (see Methods).
300 We performed simultaneous two-photon imaging and whole cell recordings of individual
301 interneurons, using an intracellular dye to trace their axons and identify presumptive presynaptic
302 boutons. Once individual boutons were identified, we triggered brief bursts of action potentials
303 and monitored iGABASnFR signals using a rapid spiral ("Tornado") scanning approach previously
304 developed for imaging glutamate sensors (Jensen et al. 2019). In interneurons expressing
305 iGABASnFR1, we were unable to detect any spike-evoked fluorescence signals, despite
306 conducting 15 trials per cell across five separate experiments (example in Fig. 6a). In contrast,
307 iGABASnFR2-expressing cells consistently displayed evoked signals at individual axonal boutons
308 (although obtaining a signal-to-noise ratio >3 might require 5-10 trial averaging; example in Fig.
309 6b).

310 We next sought to detect GABA release signals in vivo. In vivo imaging of GABA transients poses
311 additional challenges due to overlapping biological and instrumental noise sources, making
312 detection at single boutons more difficult than in quiescent brain slices. However, GABA released
313 from interneuron bursts can diffuse tens of microns from its release sites, generating extracellular
314 "volume-transmitted" signals (Oláh et al. 2009). These GABA waves have previously been
315 detected with iGABASnFR2 in brain slices during highly synchronized, pathological network
316 discharges (Magloire et al. 2023). Here we tested whether iGABASnFR2 could resolve volume-
317 transmitted GABA release in response to physiological sensory stimulation *in vivo*.

318 We focused our imaging on areas of thalamocortical input in the barrel cortex L1-L3, and applied
319 rhythmic whisker stimulation (RWS), a paradigm known to evoke reliable Ca^{2+} signals in
320 thalamocortical axons (Petreanu et al. 2012), also shown in our own prior work (Henneberger et
321 al. 2020). Following expression of AAV9-hSyn-iGABASnFR2 in cortical neurons, a brief RWS
322 protocol (four 20 Hz air puffs over 200 ms) consistently triggered robust fluorescence increases
323 across a ~150 µm-wide area in the barrel cortex layers L2-L3 (see Fig. 6c, or L1-L2 layers, Fig. 6
324 – Figure Supplement 1). Fluorescence changes were clearly visible across sensor-expressing
325 neuronal processes, consistent with the interpretation that these are volume transmitted signals
326 generated by interneurons. Based on prior calibration of iGABASnFR2 in brain slices (Magloire

et al. 2023), the observed $\Delta F/F_0$ corresponds to a transient extracellular GABA concentration increase of approximately 2–2.5 μM at peak.

Discussion

Here we report an improved GABASnFR, developed using a high throughput mutagenesis and screening pipeline that has previously been used to optimize calcium indicators (Wardill et al. 2013; Dana et al. 2016; Zhang et al. 2023). Despite the fact that only 20% of primary cultured neurons are expected to be inhibitory (Wonders & Anderson 2006), this pipeline was still capable of identifying improved sensor variants. iGABASnFR2 has a 7-fold increase in affinity for GABA, as well as a 20% increase in kinetics compared to the first-generation sensor. Importantly, sensor affinity remains in a range where it is not likely to be saturated by tonic levels of GABA. Additionally, the improved kinetics make it more likely the sensor can capture the rapid changes in GABA concentration that occur at the synaptic cleft as GABA is released and rapidly reuptaken.

The throughput of the screening platform made it possible to target 39 different sites in the protein for saturation mutagenesis. Such an extensive screen was important to get enough coverage that many sites with relatively small improvements could be combined to derive an overall more effective sensor. Of the 39 sites targeted, we found 12 mutations across 6 sites that contributed to improved sensor performance or expression. However, no single mutation produced an especially large improvement in performance. It was particularly challenging to identify single site variants with both strong expression and high signal-to-noise. Fortunately, many of the single site mutations interacted additively when combined. However, it was also the case that many double mutant combinations failed to pass our basic quality control standards, which may indicate that the combinations resulted in a failed, non-fluorescent sensor. Whether higher-order combinations can realistically yield sensors with improved performance remains an open question—functional variants may prove even more rare when more mutations are combined, and/or the increase in performance may come in smaller increments as higher order combinations are produced.

No single mutation produced an especially large improvement in performance. Identifying single-site variants with both strong expression and high signal-to-noise was particularly challenging. Many of the single-site mutations interacted additively when combined. Still, numerous double mutant combinations failed to pass basic quality control standards, possibly indicating that the combinations produced non-functional, non-fluorescent sensors. Whether higher-order combinations can realistically yield sensors with improved performance remains an open question—functional variants may become even rarer as more mutations are added, and any performance gains may diminish with each additional layer of complexity.

The extensive screening also enabled the serendipitous discovery of negative-going sensors. Of course positive- and negative-going variants cannot be combined in a single experiment because they are the same color. However, in experiments where precisely timed GABA release is expected, replicating an observation with sensors of different polarities could increase confidence in a result, especially given that signal-to-noise remains below that of other sensors such as GCaMP and iGluSnFR.

There are several promising avenues that could be taken to further optimize iGABASnFR. First, although several sites contributed small improvements in sensor performance, we did not attempt to go much beyond two-site combinations in this study, so higher order combinations are one straightforward route to further optimization. Second, sensor expression is evidently an aspect which could be improved. We attempted to capture this in our screening criteria by measuring the fraction of responsive pixels for each variant. However this partly conflates the amplitude of the sensor's signal with its expression level, and a more direct measure of expression would be preferable. Thirdly, trafficking the sensor efficiently to the membrane is likely another point of improvement. In work with iGluSnFR (Aggarwal et al. 2023) and eLACCO (Nasu et al. 2023), a panel of different transmembrane anchors were evaluated for sensor localization, and some were found to be more effective than the PDGFR domain that anchors iGABASnFR2. Finally, the high throughput of our screening pipeline may provide sufficient training data that machine learning approaches used to further optimize jGCaMP8 (Wait et al. 2024) can be applied to iGABASnFR.

Nevertheless, the improvements we identified resulted in a qualitative advance in the ability to detect inhibition in the retina. While the first-generation sensor showed some signal, direction-selective inhibition was reliably detectable on single trials only with iGABASnFR2. This sensor has also been used to detect inhibitory transmission during epileptiform activity in hippocampal slices (Magloire et al. 2023). These are strong signals, but we showed that iGABASnFR2 is sensitive enough to detect GABA release triggered by activation of single neurons in brain slices—a critical benchmark for in vivo applicability. In intact animals, the sensor reported GABA release in somatosensory cortex in response to physiological sensory stimulation. These signals reflect relatively slow volume-transmitted extracellular GABA "waves" that result from spatiotemporal summation and dissipation of multiple GABA hotspots generated by rapid GABA release at individual synapses (Oláh et al. 2009; Boddum et al. 2016; Sylantyev et al. 2020; Pavlov et al. 2014). Although we did not distinguish synaptic from extrasynaptic GABA in this study, further improvements in kinetics and signal-to-noise may be needed to reliably resolve synaptic events and broaden the utility of the sensor for more demanding in vivo applications. Even in its current form, however, iGABASnFR2 is well suited for contexts where GABA signals are spatially integrated or temporally averaged, such as photometry or strong population-level activity. Given the longstanding difficulty of directly visualizing inhibitory signaling in the brain, we anticipate that these improved sensors will serve as valuable tools for the neuroscience community.

398 **Methods**

399 *Animal care and use statement*

400 All surgical and experimental procedures involving animals were performed in accordance with
401 protocols approved by the Institutional Animal Care and Use Committee at the respective institute
402 (HHMI Janelia Research Campus, National Institute of Genetics). Procedures in the United
403 States conform to the National Institutes of Health (NIH) Guide for the Care and Use of
404 Laboratory Animals. All animal procedures in the UK were conducted in accordance with the
405 European Commission Directive (86/609/ EEC), the United Kingdom Home Office (Scientific
406 Procedures) Act (1986), with project approval from the Institutional Animal Care and Use
407 Committees of the University College London. Procedures in Japan were approved by the animal
408 experimentation committee at the National Institute of Genetics. Mice were housed under
409 controlled temperature (roughly 21°C) and humidity (roughly 50%) conditions under a reverse
410 light cycle. This research has complied with all applicable ethical regulations.

411 *Mutagenesis*

412 Site-directed mutagenesis was carried out using overlapping PCR amplicons with degenerate
413 oligonucleotide primers (NNS). A single-site NNS library (n=96) was created for each amino acid
414 residue of interest and cloned using Gibson assembly. Subsequently, top single-site variants (12
415 mutations across 6 AA sites) were assembled using overlapping amplicons to achieve all possible
416 combinations of mutations (n= 635 sequence verified variants). For neuronal screening,
417 iGABASnFR variants were cloned into an expression vector containing the CAG promoter, the
418 variant of interest, and finally a woodchuck hepatitis virus post-transcriptional regulatory element
419 (WPRE).

420 *Neuronal cell culture*

421 The primary rat culture procedure was performed largely as previously described (Dana et al.
422 2016; Wardill et al. 2013). Briefly, neonatal rat pups (Charles River Laboratory) were euthanized
423 and neocortices were dissociated and processed to form a cell pellet. Cells were resuspended
424 and transfected by combining $5x10^5$ viable cells with 400 ng plasmid DNA and nucleofection
425 solution in a 25 µL electroporation cuvette (Lonza). Electroporation of iGABASnFR mutants was
426 performed according to the manufacturer's protocol. Typically, 8 wells in a 96-well plate were
427 electroporated with iGABASnFR1 control, and 18 different mutants were electroporated into 4
428 wells each for a total of 80 wells. The first and last columns of the plate were not used because
429 pilot experiments indicated that cells grown in these wells exhibited poor health.

430 *Field stimulation assay*

431 The field stimulation assay was adapted from our existing GECI screening pipeline (Dana et al.
432 2016; Dana et al. 2019). Neurons were plated onto poly-D-lysine-coated, 96-well, glass bottom
433 plates (MatTek) at ~$1x10^5$ cells per well in 100 µL of a 1:4 mixture of NbActiv4 (BrainBits) and
434 plating medium (28 mM glucose, 2.4 mM NaHCO3, 100 µg/mL transferrin, 25 µg/mL insulin, 2
435 mM L-glutamine, 100 U/mL penicillin, 10 µg/mL streptomycin, 10% FBS in MEM), and placed in
436 an incubator at 37˚C and 5% CO_2. On the following day, 190 µL of NbActiv4 medium was added
437 to each well, and incubation continued for a total of 12-15 days.

438 For imaging, neuronal culture growth medium was exchanged three times with imaging buffer
439 (145 mM NaCl, 2.5 mM KCl, 10 mM glucose, 10 mM HEPES pH 7.4, 2 mM CaCl2, 1 mM MgCl2)
440 and imaged in 75 µL of imaging buffer and drugs (10 µM CNQX, 10 µM (R)-CPP, 10 µM gabazine,
441 1 mM (S)-MCPG, Tocris). Fluorescence time-lapse images were collected on an Olympus IX81
442 microscope using a 10x 0.4 NA objective (UPlanSApo, Olympus) and an ET-GFP filter cube
443 (Chroma #49002). Illumination was provided by a 470 nm LED (Cairn Research) and
444 fluorescence was collected by an EMCCD camera (Ixon Ultra DU897, Andor) with 256 x 256 pixel
445 frames taken at 50 Hz, with 2x binning, over a 0.8 mm x 0.8 mm FOV. A custom platinum electrode
446 was lowered into each well via a linear actuator and neurons were stimulated (1, 10, 40 pulses at
447 83 Hz, 40 V, 1 ms pulse duration; S-48, Grass Instruments) as time-lapse imaging was performed.

448 The time-lapse images were analyzed to quantify the responses of the mutants to electrical
449 stimulation. Photobleaching was corrected by fitting a single exponential to the beginning and end
450 of the recording (avoiding the response window). For each pixel in the movie, a Mann-Whitney U
451 test was performed between 1.5 sec preceding the field stimulation and 0.4 sec afterwards. Pixels
452 with a p-value < 0.01 for any of those tests were considered to be responsive. The number of
453 responsive pixels was used as a proxy for sensor expression. In the screening phase,
454 measurements of sensitivity (ΔF/F) and kinetics were performed on pooled responsive pixels from
455 each plate, and wells with < 4 responsive pixels were discarded. To account for batch variability,
456 the response of each variant was normalized to the in-plate iGABASnFR1 control.

457 Quality control on every plate was performed initially by evaluating culture conditions and
458 manually examining images from each well. General criteria for retesting were: aberrantly low
459 expression, significant clumps of unhealthy cells or sparse cell distribution, out-of-range media
460 pH, or data acquisition failures in the automated steps for focusing and field stimulus delivery.
461 Individual variants with fewer than three replicates meeting quality criteria were flagged for
462 retesting. If control iGABASnFR1 wells were flagged, the entire plate was rejected for potential
463 systemic issues and all variants were retested. Overall, 54 plates did not pass this initial quality
464 control step, and were re-screened. Subsequently, all variants with < 1,800 responsive pixels per
465 plate (representing 0.6% of all pixels) were eliminated from analysis.

466 *Protein expression and purification*
467 iGABASnFR variants of interest were expressed in *E. coli* T7 Express cells (New England
468 BioLabs) in 100 mL cultures, pelleted by centrifugation, and frozen overnight. Cells were lysed by
469 resuspending in buffer containing 20% v/v B-PER (ThermoFisher) and 0.2 mg/mL lysozyme.
470 Lysate was sonicated, clarified by centrifugation, and purified using immobilized metal affinity
471 chromatography on 1 mL nickel-charged HisPur resin (ThermoFisher). The protein was eluted in
472 a buffer containing 100 mM imidazole and concentrated by spin concentrator (Amicon).

473 *Crystal structure determination*
474 All crystallization trials were carried out at room temperature using the hanging-drop vapor
475 diffusion method. Commercial sparse-matrix screening solutions were used in initial screens
476 (Hampton Research). 1 µL of protein solution containing 10 mg/mL of iGABASnFR2, 2 mM GABA,
477 20 mM Tris, 136 mM NaCl, pH 7.4 was mixed with 1 µL of reservoir solution and equilibrated
478 against 250 µL reservoir solution. The reservoir solution for the optimized conditions contained
479 0.2 M ammonium formate and 20% w/v polyethylene glycol 3350. Diffraction data were collected

480 at the beamline 8.2.1 at Berkeley Center for Structural Biology and processed with XDS (Kabsch
481 2010). The phase was determined by molecular replacement using MOLREP and the structure
482 of unliganded iGluSnFR precursor (PDB 6DGV) without residue 1-98, 230-248, and 358-376 as
483 the starting model. Subsequently the model was rebuilt with Buccaneer (Cowtan 2006).
484 Refinement was performed using REFMAC, followed by manual remodeling with Coot (Emsley
485 et al. 2010). Details of the crystallographic analysis and statistics are presented in Fig. 3
486 Supplementary Table 1.

487 *Affinity measurements*
488 Equilibrium binding affinities were determined by titration with serial dilutions of GABA up to 10mM
489 into 0.2 μM protein solution in PBS. Measurements were made on a Tecan Spark plate reader
490 using 490 nm excitation and 515 nm excitation at room temperature (22 °C). The fluorescence
491 data was fitted to the Hill function in GraphPad Prism to determine affinity values.

492 Competition assays (Fig. 4 - fig. supp. 2) were performed similarly, except that GABA was titrated
493 in the presence of 1 mM of a potential competing ligand (various amino acids or histamine) and
494 compared with a control (PBS).

495 *pH titrations*
496 Fluorescence intensities as a function of pH were measured in both glutamate-saturated (10 mM)
497 and glutamate-free states, and fitted with a sigmoidal binding function to determine the apparent
498 pKa and apparent ΔF/F as a function of pH. The sigmoidal binding function used was fit using
499 Graphpad Prism v.10 software: F = Fmin + (Fmax−Fmin)/(1+10^(pKa−pH)), where F is the
500 observed brightness, the parameters Fmax and Fmin are limit brightnesses at high and low pH,
501 and pKa is the apparent pKa of the indicator.

502 *On-cell affinity measurements in neuronal culture*
503 To measure the EC_{50} of different sensor variants in culture conditions, neurons were transfected
504 and plated in glass-bottom 24-well plates (Mattek) as described above. After 7 days in culture,
505 they were imaged using a 20× 0.45 NA objective (LUCPlanFL N, Olympus). GABA was perfused
506 into each well using a custom 3D-printed part that held an inlet and outlet perfusion tube. The
507 inlet tube was connected to a 4-channel gravity perfusion system (VC3, ALA Scientific), and the
508 outlet tube was connected to a vacuum trap. Increasing concentrations of GABA from 0.1 μM to
509 10 mM were perfused into the culture for 5 s, followed by 9 s of GABA-free buffer, as imaging was
510 performed.

511 *Stopped-flow kinetic measurements*
512 GABA binding kinetics were measured using an Applied Photophysics SX20 stopped-flow
513 spectrometer by rapidly mixing equal volumes of dilute purified sensor protein with varying GABA
514 concentrations in PBS buffer. Fluorescence changes were detected using 490 nm excitation and
515 a 515 nm long pass filter. Measurements were taken at room temperature (22 °C). Three replicate
516 measurements were performed for each set of conditions, and reaction traces were fitted to a
517 monoexponential function in Matlab.

518 *One-photon photophysical measurements*
519 All measurements were performed on solutions of purified protein (1 to 5 μM) in 1X PBS (pH 7.3)
520 with 0 mM (apo) and 10 mM (sat) added GABA. Absorbance measurements were performed

521 using UV-Vis spectrometer (Cary 100, Agilent technologies) and fluorescence excitation-emission
522 spectra were measured using a fluorescence spectrometer (Cary Eclipse, Varian Inc.). Excitation
523 scans ranged from 250 to 530 nm and emission scans performed from 470 to 700 nm. ΔF/F,
524 defined as difference in fluorescence from proteins +/- 10 mM GABA, was calculated from the
525 fluorescence emission spectra. Quantum yield measurements were performed via the relative
526 method, using fluorescein dye (QY = 0.90 in 0.1M NaOH) as a reference. Extinction coefficient
527 measurements were determined using the alkali denaturation method, using the extinction
528 coefficient of denatured GFP as a reference (ε = 44000 M-1 cm-1 at 447 nm).

529 *Two-photon measurements*
530 Two-photon excitation spectra were measured as previously described (Akerboom et al. 2012).
531 Protein solutions (1 to 5 μM) +/- 10 mM GABA were prepared and measured using an inverted
532 microscope (IX81, Olympus) equipped with a 60× 1.2 NA water immersion objective (Olympus).
533 Two-photon excitation was achieved using an 80 MHz Ti-Sapphire laser (Chameleon Ultra II,
534 Coherent) for spectra from 710 nm to 1080 nm. Fluorescence collected through the objective
535 was passed through a short pass filter (720SP, Semrock) and a band pass filter (550BP200,
536 Semrock), before being detected by a fiber-coupled Avalanche Photodiode (APD)
537 (SPCM_AQRH-14, Perkin Elmer). The obtained two-photon excitation spectra were normalized
538 for 1 μM concentration and further used to obtain action cross-section spectra (AXS) with
539 fluorescein as a reference (Average AXS from (Xu & Webb 1996; Makarov et al. 2008).

540 *Imaging direction-selective activity in the retina*
541 We injected AAVs encoding iGABASnFR1 (ssAAV-1/2-hSyn-FLEX.iGABASnFR.F102G) and
542 iGABASnFR2.0 (ssAAV-9/2-hSyn1-dlox-iGABASnFR2(rev)-dlox-WPRE-SV40p(A)) into ChAT-
543 IRES-Cre mice to monitor the activity of starburst amacrine cells. 6-8 weeks after injection, we
544 dissected retinae and performed two-photon imaging.

545 We used two types of visual stimuli: 1) Static flash: a spot with 500 μm diameter, 100% contrast,
546 2s duration (Fig. 2d,g); 2) Moving spot, a spot with 500 μm diameter, 800 μm/s (Fig. 2e,h).

547 To quantify the response amplitude, we computed response amplitude index (RAI):

548 $$RAI = (r_s - r_b)/(r_s + r_b)$$

549 where r_s denotes the peak ΔF/F0 during visual stimulation and r_b is the mean ΔF/F0 before
550 stimulation.

551 To evaluate the response reliability, we examine the trial-to-trial variance of the signals (Baden et
552 al. 2016),

553 $$Var[\langle C\rangle_r]_t/\langle Var[C]_t\rangle_r$$

554 where C is a matrix constructed of response ΔF(t) in all stimulus trials, and $\langle\rangle_x$ and $Var[]_x$ denote
555 the mean and variance across the indicated dimension x. If all responses are identical across all
556 stimulus trials, reliability is equal to 1.

557 The signal-to-noise ratio (SNR) of motion responses was quantified as the response strength
558 relative to the variance in baseline,

559 $$SNR = (R_p - SD_b)/(R_p + SD_b)$$

560 where R_p denotes response amplitude in the preferred direction and SD_b is the standard deviation
561 of the signal before stimulation.

562 The circular variance (CV) is computed to quantify directional tuning:

563 $$CV = \left|(\Sigma_d R_d e^{i2\theta_d})/(\Sigma_d R_d)\right|$$

564 where R_d denotes response in direction d, and θ_d denotes angle in direction d.

565 *Viral transduction of iGABASnFR for acute slice experiments*
566 We used viral transduction of the optical GABA sensor in C57BL/6J mice (Charles River
567 Laboratories), as detailed earlier (Henneberger et al. 2020; Magloire et al. 2023). Briefly, an AAV
568 virus expressing iGABASnFR (Janelia Research Campus) was injected into the hippocampus
569 during aseptic surgery. The animal, secured in a stereotaxic frame and under a stable
570 anaesthesia level (maintenance at 1.5-2.5% isoflurane, body temperature maintained at
571 ~37.0°C), received perioperative analgesics (subcutaneous buprenorphine, 60 µg kg-1), and a
572 craniotomy of approximately 1 mm diameter was performed using a high-speed drill. Stereotactic
573 coordinates were 2.5 mm of the anteroposterior distance from bregma to lambda and 2.5 mm
574 lateral to the midline. Pressure injections of the sensor (totalling 0.1E10 genomic copies in a
575 volume not exceeding 200 nL) were stereotactically guided to a depth of 2.6 mm ventral from the
576 cortical surface, at a rate of approximately 1 nL sec-1. Metacam (1 mg kg-1) and saline (0.5 ml)
577 were subcutaneously administered.

578 Acute hippocampal slices (350 µm thick) were prepared from mice 3 to 5 weeks after in vivo
579 transduction. Brains were rapidly extracted and sliced in ice-cold cutting solution containing (in
580 mM): 75 NaCl, 80 sucrose, 2.5 KCl, 7 $MgCl_2$, 1.25 NaH_2PO_4, 0.5 $CaCl_2$, 26 $NaHCO_3$, 1.3 ascorbic
581 acid, 3 sodium pyruvate, and 6 glucose (osmolarity 300–305 mOsm). Slices were incubated at
582 34 °C in the same solution for 15 minutes, then transferred to an interface chamber containing
583 artificial cerebrospinal fluid (aCSF) composed of (in mM): 126 NaCl, 26 $NaHCO_3$, 2.5 KCl, 2
584 $CaCl_2$, 1.3 $MgSO_4$, 1 NaH_2PO_4, and 10 glucose (pH 7.4, 295–305 mOsm). All solutions were
585 continuously bubbled with 95% O_2 and 5% CO_2. Slices were allowed to recover for at least 60
586 minutes prior to recording. During experiments, slices were transferred to a submersion-type
587 recording chamber and superfused with extracellular solution at 33–35 °C.

588 *Organotypic slice preparation*
589 Organotypic hippocampal slice cultures were prepared from postnatal day 6–8 (P6–8) mice using
590 a modified version of the interface culture method (Stoppini et al. 1991). Hippocampi were
591 sectioned at 300 µm using a Leica VT1200S vibratome in ice-cold sterile slicing solution
592 containing (in mM): 105 sucrose, 50 NaCl, 2.5 KCl, 1.25 NaH_2PO_4, 7 $MgCl_2$, 0.5 $CaCl_2$, 1.3
593 ascorbic acid, 3 sodium pyruvate, 26 $NaHCO_3$, and 10 glucose. Slices were washed in culture
594 medium composed of 50% Minimal Essential Medium, 25% horse serum, 25% Hanks' Balanced
595 Salt Solution, 0.5% L-glutamine, 28 mM glucose, and antibiotics (100 U/mL penicillin and

596 100 µg/mL streptomycin). Three to four slices were placed on each 0.4 µm pore membrane insert
597 (Millicell-CM, Millipore, UK) and maintained at 37 °C in a humidified 5% CO_2 incubator. Medium
598 was exchanged every 2–3 days, and cultures were maintained for up to 21 days in vitro (DIV).
599 For electrophysiological recordings, slices were transferred to a submersion-type chamber and
600 perfused with oxygenated aCSF. Recordings were performed at 33–35 °C. To minimize plasticity-
601 related changes during prolonged recordings, the aCSF was supplemented with 10 µM NBQX
602 and 50 µM AP5.

603 *Biolistic transfection of iGABASnFR variants*
604 iGABASnFR2 was expressed under the synapsin promoter in CA3 interneurons in organotypic
605 hippocampal slice cultures using biolistic transfection techniques adapted from manufacturer's
606 instructions (Bio-Rad), as detailed earlier (Jensen et al. 2017). Gold micro-carriers (1.6 µm; 6–
607 8 mg) were coated with 30 µg of plasmid DNA. At 5 days in vitro (DIV), cultures were treated
608 overnight with culture media containing 5 µM Ara-C to reduce glial reaction following transfection.
609 The following day, slices were transfected using a Helios gene gun (Bio-Rad) at 120 psi. Cultures
610 were then returned to standard media and maintained for an additional 5–10 days before
611 recordings.

612 *Electrophysiology and Axonal Imaging in Hippocampal Slices*
613 Whole-cell patch-clamp recordings were obtained from visually identified CA1 pyramidal neurons
614 using infrared differential interference contrast (IR-DIC) microscopy. Recording electrodes were
615 fabricated from thin-walled borosilicate glass capillaries and had resistances of 2.5–3.5 MΩ. The
616 internal pipette solution contained (in mM): 135 KCH_3O_3S, 10 HEPES, 10 Na_2-phosphocreatine
617 or di-Tris-phosphocreatine, 4 $MgCl_2$, 4 Na_2-ATP, 0.4 Na-GTP, and 5 QX-314 bromide. The pH
618 was adjusted to 7.2 using KOH, and osmolarity was maintained at 290–295 mOsm. Alexa Fluor
619 594 hydrazide (50 µM) was included to visualize cell morphology and identify synaptic boutons.

620 Recordings were performed in voltage-clamp mode with cells held at −65 mV. The extracellular
621 aCSF was supplemented with 100 µM picrotoxin (Tocris Bioscience) and 30 µM D-serine.
622 Electrophysiological signals were acquired using a Multiclamp 700B amplifier (Molecular Devices)
623 and a motorized micromanipulator and XY translation stage system (Luigs and Neumann).
624 Signals were digitized at 10 kHz and stored for offline analysis using either WinWCP (versions
625 4.1.5–4.7; John Dempster, University of Strathclyde) or pCLAMP (versions 10.4–10.5; Molecular
626 Devices).

627 To visualize and trace axons of patched interneurons, we used a Femtonics Femto2D (or 3D)-
628 FLIM imaging system integrated with patch-clamp electrophysiology (Femtonics, Budapest) and
629 linked on the same light path to two femtosecond pulsed lasers MaiTai (SpectraPhysics-Newport)
630 with independent shutter and intensity control. For CA3 pyramidal cells, internal solution
631 contained (in mM) 135 potassium methane-sulfonate, 10 HEPES, 10 di-Tris-Phosphocreatine, 4
632 $MgCl_2$, 4 Na_2-ATP, and 0.4 Na-GTP (pH adjusted to 7.2 using KOH, osmolarity 290–295).
633 Presynaptic imaging was carried out using an adaptation of previously described methods for
634 separate presynaptic glutamate and Ca2+ imaging (Jensen et al. 2017).

635 iGABASnFR-expressing cells were identified using two-photon imaging at 910 nm and patched
636 in whole-cell configuration using a 25× Olympus objective (NA 1.05) for visualization. After break-

637 in, 30–45 min was allowed for Alexa Fluor 594 to equilibrate throughout the axonal arbor. Axons,
638 identified by their smooth morphology and often tortuous trajectory, were traced to their targets
639 using frame scan mode. If iGABASnFR fluorescence was too weak, we switched to the Alexa
640 channel to trace the axon using 800 nm excitation. Discrete boutons were identified using
641 established morphological criteria. Tornado scans of 1.5 micron diameter were set over the pre-
642 synaptic bouton and scanned at a rate of 500Hz with a train of action potentials initiated by brief
643 positive voltage steps. While the laser power was reduced to minimize photobleaching, any
644 detectable photobleaching trends were corrected in individual recordings a posteriori.

645 *Viral transduction of synGABASnFR2 in the barrel cortex*
646 Male and female C57BL/6N mice (1–1.5 months old) were prepared for aseptic surgery.
647 Perioperative multimodal analgesia utilized buprenorphine (60 µg kg-1, s.c.) and lidocaine (2.5%)
648 topically applied to the surgical site; ocular ointment (Lacri-lube, Allergan, UK) was applied to
649 prevent corneal drying. Anesthesia was induced with 5% isoflurane and maintained at 1.5–2.5%.
650 After shaving, the scalp was disinfected with three washes of chlorhexidine, and the mouse was
651 secured in a stereotaxic frame (David Kopf Instruments, USA). Adequate anesthesia was
652 confirmed by loss of pedal reflexes, and body temperature was maintained at ~37 °C using a
653 feedback-controlled heating system.

654 A midline incision was made and overlying soft tissue resected to expose the skull. A small
655 craniotomy (~1 mm diameter) was drilled using a high-speed dental drill at coordinates targeting
656 either the somatosensory cortex (AP: −1.5 mm, ML: −3.0 mm relative to bregma) or hippocampus
657 (AP: −1.9 mm, ML: −1.4 mm, DV: −1.35 mm). AAV9-hSyn-GABASnFR2 was injected via a
658 Hamilton syringe stereotactically positioned 1 mm below the cortical surface. Injections (300–
659 500 nL total volume) were delivered at ~20 nL/min using a microinjection pump in three steps,
660 retracting the needle by 150–200 µm after each step. After completion, the needle was left in
661 place for ~5 min before withdrawal. The wound was sutured, and animals received meloxicam
662 (1 mg/kg) and 0.5 mL saline. Recovery took place in a heated chamber, with postoperative
663 monitoring until full wound healing (typically 2–4 days).

664 *Cranial window implantation*
665 Mice were anesthetized and positioned in a stereotaxic frame as described for the viral
666 transduction procedure. Once stabilized under general anesthesia (isoflurane, maintained at 1.5–
667 2%), a large portion of the scalp was removed to expose the right frontal and parietal skull bones,
668 along with the medial regions of the left frontal and parietal bones. The right temporalis muscle
669 was reflected laterally to expose the squamous suture, to facilitate cement bonding during fixation
670 of the cranial window implant. The exposed skull surface was coated with Vetbond (3M, USA),
671 and a custom-designed headplate was mounted over the S1BF using dental cement (SuperBond,
672 Sun Medical Co. Ltd., Japan).

673 After the bonding agents had fully cured, the animal was transferred to a custom-built head fixation
674 setup. A 3 mm craniotomy was made over the right somatosensory cortex, centered over the
675 S1BF injection site, using a high-speed hand drill. After sufficiently thinning the skull, prior to
676 removal of the skull flap, the surface was superfused with warmed aCSF (in mM: 125 NaCl, 2.5
677 KCl, 26 $NaHCO_3$, 1.25 Na_2HPO_4, 10 glucose, 2 $CaCl_2$, 2 $MgSO_4$ saturated with 95% O_2 / 5% CO_2
678 pH 7.4). The skull flap was removed using fine-tipped forceps (11252-40, Fine Science Tools,

679 Germany). Immediately after opening, the brain was superfused with sterile saline. The durotomy
680 was performed using 26G needles with hand-made curved tips (modified by tapping against a
681 hard surface), ensuring the pia mater remained intact.

682 A custom-prepared cranial window—a double-glass assembly consisting of a 34 mm diameter
683 round coverglass bonded beneath a 4 mm diameter round coverglass (Harvard Apparatus UK),
684 affixed with UV-curable optical adhesive (NOA61, ThorLabs Inc., NJ, USA)—was placed over the
685 exposed cortex. Slight downward pressure was applied to the coverslip using a stereotactically
686 guided wooden spatula to prevent excessive force to the open brain surface, as described
687 previously (Henneberger et al. 2020). Superfusion was stopped, and excess aCSF was carefully
688 absorbed with a sterile surgical sponge, ensuring no fluid remained beneath the cranial window.
689 The coverslip was secured with dental cement. After completing the surgery, the anaesthesia
690 regime was switched from inhalation to i.p. injection, using a mixture of fentanyl (0.03 mg/kg),
691 midazolam (3 mg/kg), and medetomidine (0.3 mg/kg), for subsequent imaging in the
692 anaesthetised animal.

693 *Multiplexed Two-Photon imaging in vivo*
694 The animal was transferred to the Femtosmart imaging system (Femtonics, Budapest), integrated
695 with electrophysiology and connected to a tunable femtosecond pulsed laser (Insight X3, Spectra-
696 Physics/Newport) for multiplexed two-photon excitation (2PE) imaging. Under anesthesia, the
697 animal was secured on a custom-built stage via the implanted headplate, beneath an XLPlan N
698 25× water-immersion objective (NA 1.05) and illuminated with a green lamp.

699 2PE imaging was performed at 910 nm, optimized for the sensor. Imaging was conducted in
700 cortical layers 1 and 2/3 at depths ranging from 50 to 300 µm, adjusting laser intensity to minimize
701 photobleaching (<15 mW). Once a suitable region was identified, data were acquired using either
702 Tornado (spiral) linescan mode (0.5–1 kHz) or resonant frame scan mode. Frame scan time series
703 were typically recorded as 512 × 50 × 317 pixels at 200–300 Hz for 5 s. Recordings were acquired
704 using MESc v3.5.7 (Femtonics) and exported as t-stacks for further processing in ImageJ. In
705 Tornado scan mode, circular fields of view (50–150 µm in diameter) were selected to encompass
706 iGABASnFR2-positive cells. Given that GABA released from brief interneuronal bursts is
707 expected to diffuse across extracellular distances on the order of 10 µm, we opted to image
708 relatively broad imaging fields of view (50–150 µm) rather than targeting individual presynaptic
709 boutons.

710 *Statistics and reproducibility*
711 Values and errors reported throughout the text are mean ± s.e.m. unless otherwise noted.
712 Statistical analyses were performed in Graphpad Prism v.8 (in vitro photophysics), MATLAB,
713 Python and OriginPro, as described in the text.

714 *Reagent availability*
715 A variety of mammalian and bacterial expression plasmids as well as AAVs for iGABASnFR2 and
716 iGABASnFR2n are available through Addgene
717 (https://www.addgene.org/browse/article/28247749/). Requests for other reagents, such as
718 sensor variants with different affinities, can be made by contacting
719 GENIEreagents@janelia.hhmi.org.

Acknowledgements:

We thank Tim Brown from the Janelia Tool Translation Team, Deepika Walpita and Phuong Nguyen for providing resources. Work at Janelia research campus was funded by the Howard Hughes Medical Institute. A.M. was supported by funding from PRESTO JST (JPMJPR2489) and KAKENHI (23K19412). K.Y. was supported by funding from KAKENHI (20K23377; 22K21353; 23H04241; 24H02311). L.L.L. was supported by a Wellcome Collaborative Award (223131/Z/21/Z); D.A.R. was supported by funding from MRC Research Grant (ref MR/W019752/1), Wellcome Collaborative Award (223131/Z/21/Z) and BBSRC Research Grant (PI; ref BB/Y003926/1). O.K. was supported by UCL-Wellcome Trust Translational Partnership Pilot Award (RM-TIN OK: #178973). D.A.R, O.K. and T.J. thank Dr. James Reynolds for help with setting up in vivo viral transduction protocols.

731 **References**

732 Aggarwal, A. et al., 2023. Glutamate indicators with improved activation kinetics and localization
733 for imaging synaptic transmission. *Nature methods*, pp.1–10.

734 Akerboom, J. et al., 2009. Crystal structures of the GCaMP calcium sensor reveal the
735 mechanism of fluorescence signal change and aid rational design. *The Journal of biological*
736 *chemistry*, 284(10), pp.6455–6464.

737 Akerboom, J. et al., 2012. Optimization of a GCaMP calcium indicator for neural activity
738 imaging. *The Journal of neuroscience: the official journal of the Society for Neuroscience*,
739 32(40), pp.13819–13840.

740 Baden, T. et al., 2016. The functional diversity of retinal ganglion cells in the mouse. *Nature*,
741 529(7586), pp.345–350.

742 Barberis, A., Petrini, E.M. & Cherubini, E., 2004. Presynaptic source of quantal size variability at
743 GABAergic synapses in rat hippocampal neurons in culture. *The European journal of*
744 *neuroscience*, 20(7), pp.1803–1810.

745 Boddum, K. et al., 2016. Astrocytic GABA transporter activity modulates excitatory
746 neurotransmission. *Nature communications*, 7(1), p.13572.

747 Briggman, K.L., Helmstaedter, M. & Denk, W., 2011. Wiring specificity in the direction-selectivity
748 circuit of the retina. , 471(7337), pp.183–188.

749 Cowtan, K., 2006. TheBuccaneersoftware for automated model building. 1. Tracing protein
750 chains. *Acta crystallographica. Section D, Biological crystallography*, 62(9), pp.1002–1011.

751 Dana, H. et al., 2019. High-performance calcium sensors for imaging activity in neuronal
752 populations and microcompartments. *Nature Publishing Group*, 16(7), pp.649–657.

753 Dana, H. et al., 2016. Sensitive red protein calcium indicators for imaging neural activity. *eLife*,
754 5. Available at: http://dx.doi.org/10.7554/eLife.12727.

755 Ding, J. et al., 2014. Structural basis of the ultrasensitive calcium indicator GCaMP6. *Science*
756 *China. Life sciences*, 57(3), pp.269–274.

757 Dong, C. et al., 2022. Fluorescence Imaging of Neural Activity, Neurochemical Dynamics, and
758 Drug-Specific Receptor Conformation with Genetically Encoded Sensors. *Annual review of*
759 *neuroscience*, 45, pp.273–294.

760 Emsley, P. et al., 2010. Features and development of Coot. *Acta Crystallographica Section D:*
761 *Biological Crystallography*, 66(4), pp.486–501.

762 Euler, T., Detwiler, P.B. & Denk, W., 2002. Directionally selective calcium signals in dendrites of
763 starburst amacrine cells. *Nature*, 418(6900), pp.845–852.

764 Glykys, J. & Mody, I., 2007. The main source of ambient GABA responsible for tonic inhibition in
765 the mouse hippocampus: The main source of ambient GABA. *The journal of physiology*,
766 582(Pt 3), pp.1163–1178.

767 Henneberger, C. et al., 2020. LTP induction boosts glutamate spillover by driving withdrawal of

768 perisynaptic astroglia. *Neuron*, 108(5), pp.919–936.e11.

769 Jensen, T.P. et al., 2017. Monitoring single-synapse glutamate release and presynaptic calcium
770 concentration in organised brain tissue. *Cell calcium*, 64, pp.102–108.

771 Jensen, T.P. et al., 2019. Multiplex imaging relates quantal glutamate release to presynaptic
772 Ca2+ homeostasis at multiple synapses in situ. *Nature communications*, 10(1), p.1414.

773 Kabsch, W., 2010. XDS. *Acta crystallographica. Section D, Biological crystallography*, 66(Pt 2),
774 pp.125–132.

775 Lerma, J. et al., 1986. In vivo determination of extracellular concentration of amino acids in the
776 rat hippocampus. A method based on brain dialysis and computerized analysis. *Brain*
777 *research*, 384(1), pp.145–155.

778 Looger, L.L. & Griesbeck, O., 2012. Genetically encoded neural activity indicators. *Current*
779 *opinion in neurobiology*, 22(1), pp.18–23.

780 Macdonald, R.L. & Olsen, R.W., 1994. GABAA receptor channels. *Annual review of*
781 *neuroscience*, 17(1), pp.569–602.

782 Magloire, V. et al., 2023. Volume-transmitted GABA waves pace epileptiform rhythms in the
783 hippocampal network. *Current biology: CB*, 33(7), pp.1249–1264.e7.

784 Makarov, N.S., Drobizhev, M. & Rebane, A., 2008. Two-photon absorption standards in the 550-
785 1600 nm excitation wavelength range. *Optics express*, 16(6), pp.4029–4047.

786 Marvin, J.S. et al., 2019. A genetically encoded fluorescent sensor for in vivo imaging of GABA.
787 *Nature methods*, 16(8), pp.763–770.

788 Marvin, J.S. et al., 2011. A genetically encoded, high-signal-to-noise maltose sensor. *Proteins*,
789 79(11), pp.3025–3036.

790 Marvin, J.S. & Hellinga, H.W., 2001. Manipulation of ligand binding affinity by exploitation of
791 conformational coupling. *Nature structural biology*, 8(9), pp.795–798.

792 Mozrzymas, J.W. et al., 2003. Modulation of GABA(A) receptors by hydrogen ions reveals
793 synaptic GABA transient and a crucial role of the desensitization process. *The Journal of*
794 *neuroscience: the official journal of the Society for Neuroscience*, 23(22), pp.7981–7992.

795 Nasu, Y. et al., 2023. Lactate biosensors for spectrally and spatially multiplexed fluorescence
796 imaging. *Nature communications*, 14(1), p.6598.

797 Oláh, S. et al., 2009. Regulation of cortical microcircuits by unitary GABA-mediated volume
798 transmission. *Nature*, 461(7268), pp.1278–1281.

799 Pavlov, I. et al., 2014. Tonic GABAA conductance bidirectionally controls interneuron firing
800 pattern and synchronization in the CA3 hippocampal network. *Proceedings of the National*
801 *Academy of Sciences of the United States of America*, 111(1), pp.504–509.

802 Petreanu, L. et al., 2012. Activity in motor-sensory projections reveals distributed coding in
803 somatosensation. *Nature*, 489(7415), pp.299–303.

Planamente, S. et al., 2010. A conserved mechanism of GABA binding and antagonism is revealed by structure-function analysis of the periplasmic binding protein Atu2422 in Agrobacterium tumefaciens. *The journal of biological chemistry*, 285(39), pp.30294–30303.

Planamente, S. et al., 2012. Structural basis for selective GABA binding in bacterial pathogens: Structure and function of a selective GABA sensor. *Molecular microbiology*, 86(5), pp.1085–1099.

Quiocho, F.A. & Ledvina, P.S., 1996. Atomic structure and specificity of bacterial periplasmic receptors for active transport and chemotaxis: variation of common themes. *Molecular microbiology*, 20(1), pp.17–25.

Roth, F.C. & Draguhn, A., 2012. GABA metabolism and transport: effects on synaptic efficacy. *Neural plasticity*, 2012, p.805830.

Sohal, V.S. & Rubenstein, J.L.R., 2019. Excitation-inhibition balance as a framework for investigating mechanisms in neuropsychiatric disorders. *Molecular psychiatry*, 24(9), pp.1248–1257.

Stoppini, L., Buchs, P.A. & Muller, D., 1991. A simple method for organotypic cultures of nervous tissue. *Journal of neuroscience methods*, 37(2), pp.173–182.

Sylantyev, S. et al., 2020. Extracellular GABA waves regulate coincidence detection in excitatory circuits. *The journal of physiology*, 598(18), pp.4047–4062.

Telmer, P.G. & Shilton, B.H., 2003. Insights into the conformational equilibria of maltose-binding protein by analysis of high affinity mutants. *The journal of biological chemistry*, 278(36), pp.34555–34567.

Tossman, U., Jonsson, G. & Ungerstedt, U., 1986. Regional distribution and extracellular levels of amino acids in rat central nervous system. *Acta physiologica Scandinavica*, 127(4), pp.533–545.

Vaney, D.I., Sivyer, B. & Taylor, W.R., 2012. Direction selectivity in the retina: symmetry and asymmetry in structure and function. *Nature reviews. Neuroscience*, 13(3), pp.194–208.

Wait, S.J. et al., 2024. Machine learning-guided engineering of genetically encoded fluorescent calcium indicators. *Nature computational science*, 4(3), pp.224–236.

Wardill, T.J. et al., 2013. A Neuron-Based Screening Platform for Optimizing Genetically-Encoded Calcium Indicators. *PloS one*, 8(10), p.e77728.

Wonders, C.P. & Anderson, S.A., 2006. The origin and specification of cortical interneurons. *Nature reviews. Neuroscience*, 7(9), pp.687–696.

Xu, C. & Webb, W.W., 1996. Measurement of two-photon excitation cross sections of molecular fluorophores with data from 690 to 1050 nm. *Journal of the Optical Society of America. B, Optical physics*, 13(3), p.481.

Yang, Y., Li, B. & Li, Y., 2024. Genetically encoded sensors for the in vivo detection of neurochemical dynamics. *Annual review of analytical chemistry (Palo Alto, Calif.)*, 17(1), pp.367–392.

Yonehara, K. et al., 2011. Spatially asymmetric reorganization of inhibition establishes a motion-sensitive circuit. *Nature*, 469(7330), pp.407–410.

van der Zeyden, M. et al., 2008. Microdialysis of GABA and glutamate: analysis, interpretation and comparison with microsensors. *Pharmacology, biochemistry, and behavior*, 90(2), pp.135–147.

Zhang, Y. et al., 2023. Fast and sensitive GCaMP calcium indicators for imaging neural populations. *Nature*, 615(7954), pp.884–891.

850 ## Figure Legends

851 **Figure 1. Field stimulation screen for improved iGABASnFR.**

852 **a**. Top: Schematic representation of iGABASnFR1 and the amino acid substitutions that gave rise
853 to iGABASnFR2 and iGABASnFR2n. White, IgG secretion signal (cleaved off during trafficking
854 to cell surface); blue, GABA binding protein Pf622; green, cpSFGFP; dark green, Myc epitope
855 tag; red, PDGFR transmembrane domain. Numbering is relative to each of the constituent protein
856 domains; the relationship to sequential numbering of the entire polypeptide is shown in **Figure 1**
857 **- figure supplement 1**.

858 Bottom: Crystal structure of a preliminary version of iGABASnFR (PDB ID 6DGV) with the 39 sites
859 targeted for mutagenesis. Gray spheres indicate the approximate position of GABA, based on
860 homology to the liganded structure of GABA-binding protein Atu4243 (Planamente et al. 2012).

861 **b**. Mutagenesis and screening strategy. Variants with single site mutations are screened for ΔF/F
862 and expression in an initial field stimulation assay, strong performers identified and then combined
863 and re-screened in a second round. The top-performing mutants (positive-going quadruple mutant
864 iGABASnFR2 and negative-going triple mutant iGABASnFR2n) are characterized further.

865 **c**. Joint optimization of sensitivity (ΔF/F, x-axis) and expression, measured with responsive pixels
866 (y-axis). ΔF/F is normalized to in-plate iGABASnFR1 controls. Black circle: (1,1) position
867 represents iGABASnFR. Plus signs: mutants from the first round that were put together to form
868 combos in the second round. iGABASnFR2 and 2n exhibited increased ΔF/F (4.3-fold and -2.2-
869 fold of iGABASnFR, respectively) and greater numbers of responsive pixels (13.1-fold and 10.3-
870 fold). Illumination: 0.34 mW/mm^2, imaging framerate: 50 Hz.

871 **d**. Performance measures of sensor variants from the screen. Single site variants shown in gray,
872 double site combinations shown in black. Variants are ranked according to the ΔF/F0 values
873 measured for 40 AP, and those rankings maintained for the lower displays of sensor F0, tau on,
874 the time constant of the rising phase of the response, and tau off for the decay. All values are
875 normalized to in-plate iGABASnFR1 controls.

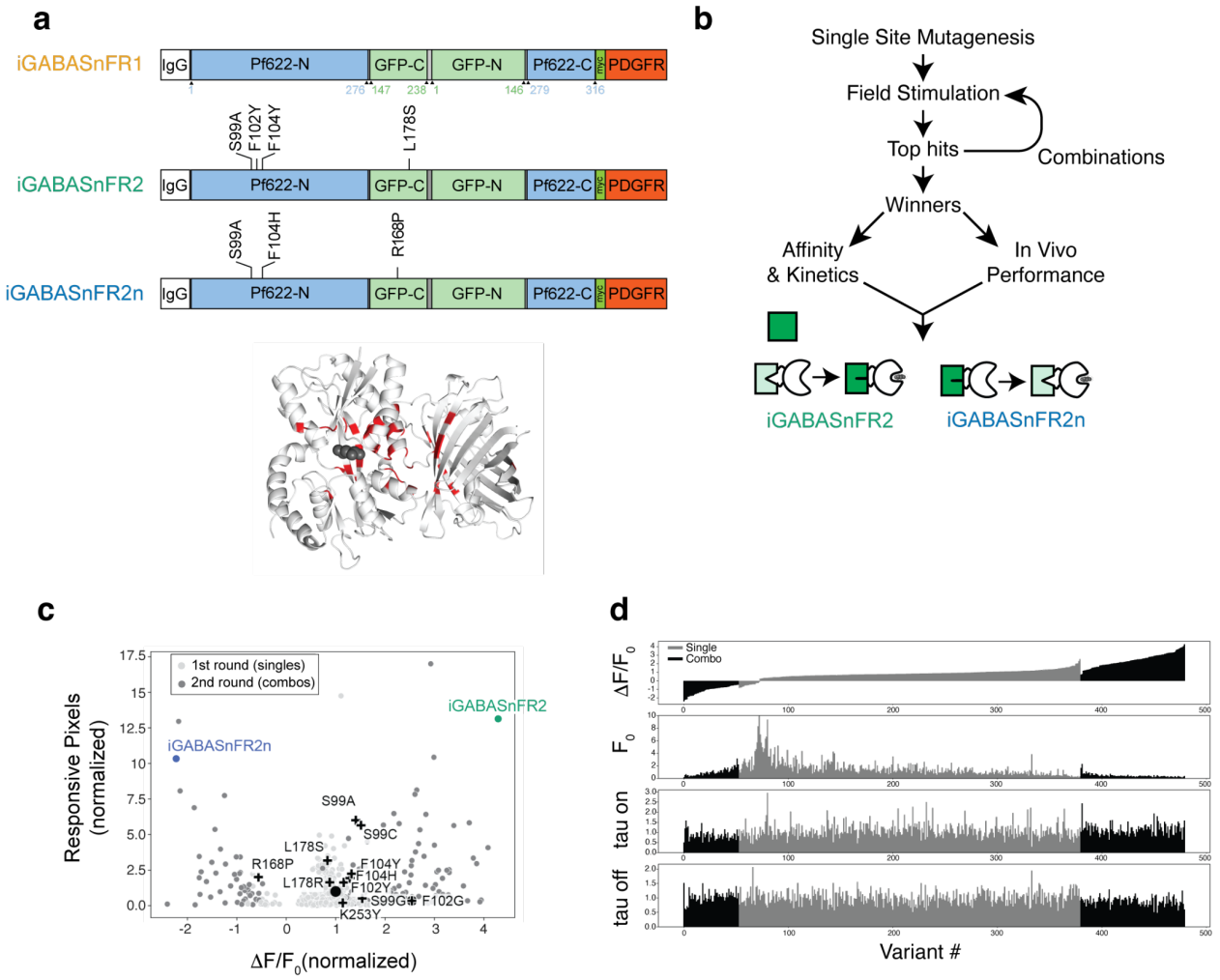
a
iGABASnFR1
IgG
Pf622-N
GFP-C
GFP-N
Pf622-C
PDGFR
iGABASnFR2
S99A
F102Y
F104Y
L178S
iGABASnFR2n
S99A
F104H
R168P
b
Single Site Mutagenesis
Field Stimulation
Top hits
Combinations
Winners
Affinity & Kinetics
In Vivo Performance
iGABASnFR2
iGABASnFR2n
c
1st round (singles)
2nd round (combos)
iGABASnFR2
iGABASnFR2n
S99A
S99C
L178S
R168P
F104Y
F104H
L178R
F102Y
S99G
F102G
K253Y
Responsive Pixels (normalized)
ΔF/F0(normalized)
d
Single
Combo
ΔF/F0
F0
tau on
tau off
Variant #

876

Figure 1

877 **Figure 1 - figure supplement 1.**

878 **a.** Annotated amino acid sequence of iGABASnFRs. iGABASnFR1 sequence shown in gray text,
879 with sites targeted for mutagenesis in black.

880 Shading indicates domains according to:
881 IgG secretion signal
882 Pf622 2-276
883 SFGFP 147-238 Junction SFGFP 1-146
884 Pf622 277-320
885 Myc epitope
886 PDGFR transmembrane domain 513-561

887 **b.** iGABASnFR2 sequence, with mutations shown in red text. Mutations are listed according to
888 domain numbers, with sequential numbering through the polypeptide indicated at the left.

889 Sequential numbering through the polypeptide is indicated on the left, while mutations in the text
890 are listed according to domain numbers: $S99_{Pf}A.F102_{Pf}Y.F104_{Pf}Y.L178_{gfp}S$.

891 $S99_{Pf}A.F102_{Pf}Y.F104_{Pf}Y.L178_{gfp}S$, which we subsequently refer to as iGABASnFR2, and the best
892 variant with inverted signal, iGABASnFR.$S99_{Pf}A.F104_{Pf}H.R168_{gfp}P$ was chosen to be
893 iGABASnFR2n.

894 **c.** iGABASnFR2n sequence, with mutations shown in red text. Sequential numbering through the
895 polypeptide is indicated on the left, while mutations in the text are listed according to domain
896 numbers: $S99_{Pf}A.F104_{Pf}H.R168_{gfp}P$.

897 **d.** Schematic showing the relationship between domain-based numbering scheme and sequential
898 numbering through the entire polypeptide (top) and the domain-based numbering scheme. In
899 both schemes numbering starts at the residue exposed after signal sequence cleavage.

IgG secretion signal
Pf622 2-276
SFGFP 147-238 Linker SFGFP 1-146
Pf622 277-320
Myc epitope
PDGFR transmembrane domain 513-561

iGABASnFR1

```
  1 METDTLLLWV LLLWVPGSTG DRSESINFVS WGGSTQDAQK QAWADPFSKA SGITVVQDGP
 61 TDYGKLKAMV ESGNVQWDVV DVEADFALRA AAEGLLEPLD FSVIQRDKID PRFVSDHGVG
121 SFLFSFVLGY NEGKLGASKP QDWTALFDTK TYPGKRALYK WPSPGVLELA LLADGVPADK
181 LYPLDLDRAF KKLDTIKKDI VWWGGGAQSQ QLLASGEVSM GQFWNGRIHA LQEDGAPVGV
241 SWKQNLVMAD ILVVPKGTKN KAAAMKFLAS ASSAKGQDDF SALTAYAPVN IDSVQRLDLA
301 QVRITADKQK NGIMANFKIR HNVEDGSVQL ADHYQQNTPI GDGPVLLPDN HYLSTQSVLS
361 KDPNEKRDHM VLLEFVTAAG ITLGMDELYK GGTGGSMSKG EELFTGVVPI LVELDGDVNG
421 HKFSVRGEGE GDATNGKLTL KFICTTGKLP VPWPTLVTTL TYGVQCFSRY PDHMKQHDFF
481 KSAMPEGYVQ ERTISFKDDG TYKTRAEVKF EGDTLVNRIE LKGIDFKEDG NILGHKLEYN
541 WNANLAPNLP TAYVKDQITL DFAYWAKNGP AIATRWNEWL VKLQVDEQKL ISEEDLNAVG
601 QDTQEVIVVP HSLPFKVVVI SAILALVVLT IISLIILIML WQKKPR*
```

iGABASnFR2

```
  1 METDTLLLWV LLLWVPGSTG DRSESINFVS WGGSTQDAQK QAWADPFSKA SGITVVQDGP
 61 TDYGKLKAMV ESGNVQWDVV DVEADFALRA AAEGLLEPLD FSVIQRDKID PRFVSDHGVG
121 AFLYSYVLGY NEGKLGASKP QDWTALFDTK TYPGKRALYK WPSPGVLELA LLADGVPADK
181 LYPLDLDRAF KKLDTIKKDI VWWGGGAQSQ QLLASGEVSM GQFWNGRIHA LQEDGAPVGV
241 SWKQNLVMAD ILVVPKGTKN KAAAMKFLAS ASSAKGQDDF SALTAYAPVN IDSVQRLDLA
301 QVRITADKQK NGIMANFKIR HNVEDGSVQS ADHYQQNTPI GDGPVLLPDN HYLSTQSVLS
361 KDPNEKRDHM VLLEFVTAAG ITLGMDELYK GGTGGSMSKG EELFTGVVPI LVELDGDVNG
421 HKFSVRGEGE GDATNGKLTL KFICTTGKLP VPWPTLVTTL TYGVQCFSRY PDHMKQHDFF
481 KSAMPEGYVQ ERTISFKDDG TYKTRAEVKF EGDTLVNRIE LKGIDFKEDG NILGHKLEYN
541 WNANLAPNLP TAYVKDQITL DFAYWAKNGP AIATRWNEWL VKLQVDEQKL ISEEDLNAVG
601 QDTQEVIVVP HSLPFKVVVI SAILALVVLT IISLIILIML WQKKPR*
```

iGABASnFR2n

```
  1 METDTLLLWV LLLWVPGSTG DRSESINFVS WGGSTQDAQK QAWADPFSKA SGITVVQDGP
 61 TDYGKLKAMV ESGNVQWDVV DVEADFALRA AAEGLLEPLD FSVIQRDKID PRFVSDHGVG
121 AFLFSHVLGY NEGKLGASKP QDWTALFDTK TYPGKRALYK WPSPGVLELA LLADGVPADK
181 LYPLDLDRAF KKLDTIKKDI VWWGGGAQSQ QLLASGEVSM GQFWNGRIHA LQEDGAPVGV
241 SWKQNLVMAD ILVVPKGTKN KAAAMKFLAS ASSAKGQDDF SALTAYAPVN IDSVQRLDLA
301 QVRITADKQK NGIMANFKIP HNVEDGSVQL ADHYQQNTPI GDGPVLLPDN HYLSTQSVLS
361 KDPNEKRDHM VLLEFVTAAG ITLGMDELYK GGTGGSMSKG EELFTGVVPI LVELDGDVNG
421 HKFSVRGEGE GDATNGKLTL KFICTTGKLP VPWPTLVTTL TYGVQCFSRY PDHMKQHDFF
481 KSAMPEGYVQ ERTISFKDDG TYKTRAEVKF EGDTLVNRIE LKGIDFKEDG NILGHKLEYN
541 WNANLAPNLP TAYVKDQITL DFAYWAKNGP AIATRWNEWL VKLQVDEQKL ISEEDLNAVG
601 QDTQEVIVVP HSLPFKVVVI SAILALVVLT IISLIILIML WQKKPR*
```

900

901 **Figure 2. Characterization of iGABASnFR variants in cultured neurons.**

902 **a.** Fluorescence images of primary neurons expressing iGABASnFR1 (orange), iGABASnFR2
903 (green), iGABASnFR2n (blue) under the CAG promoter at baseline, at peak brightness after field
904 stimulation with 40 APs, and the corresponding ΔF/F0. Scale bar, 20 μm.

905 **b.** Time courses of the ΔF/F0 response to 1, 10 and 40 APs delivered at 83 Hz. iGABASnFR2n
906 signals are inverted for display. Traces and error bars denote mean ± s.e.m., n = 20 culture wells
907 for each variant.

908 **c.** 10–90% rise time of the three sensor variants for the 1 AP condition.

909 **d.** Peak ΔF/F0 of the three variants over different levels of stimulation.

910 **e.** Signal-to-noise (d′) of the three variants over different levels of stimulation.

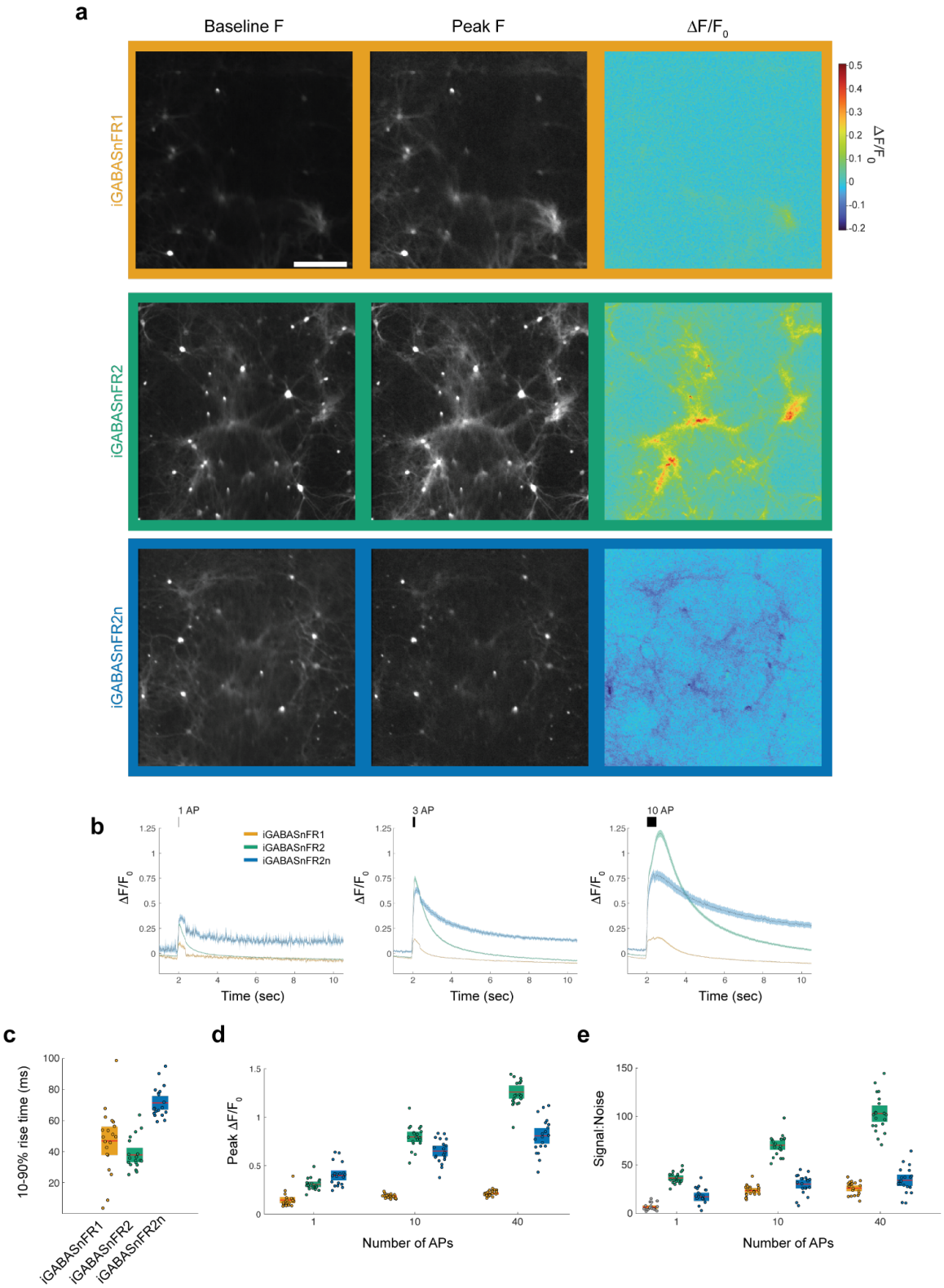
a
Baseline F
Peak F
ΔF/F0
iGABASnFR1
iGABASnFR2
iGABASnFR2n
ΔF/F0
b
1 AP
3 AP
10 AP
iGABASnFR1
iGABASnFR2
iGABASnFR2n
ΔF/F0
Time (sec)
c
10-90% rise time (ms)
iGABASnFR1
iGABASnFR2
iGABASnFR2n
d
Peak ΔF/F0
Number of APs
e
Signal:Noise
Number of APs

Figure 2

913 **Figure 3. Crystal structure of iGABASnFR2 in complex with GABA**

914 **a.** Superposition of the structure of iGABASnFR2 in complex with GABA (cyan) and unliganded
915 iGABASnFR precursor (magenta). The bound GABA molecule is represented as colored spheres.

916 **b.** Cartoon representation of iGABASnFR2 with key mutations shown as yellow sticks. Mutations
917 in the original iGABASnFR1 shown in orange.

918 **c.** GABA binding site of iGABASnFR2. Residues involved in GABA binding are shown as lines
919 and GABA shown as stick.

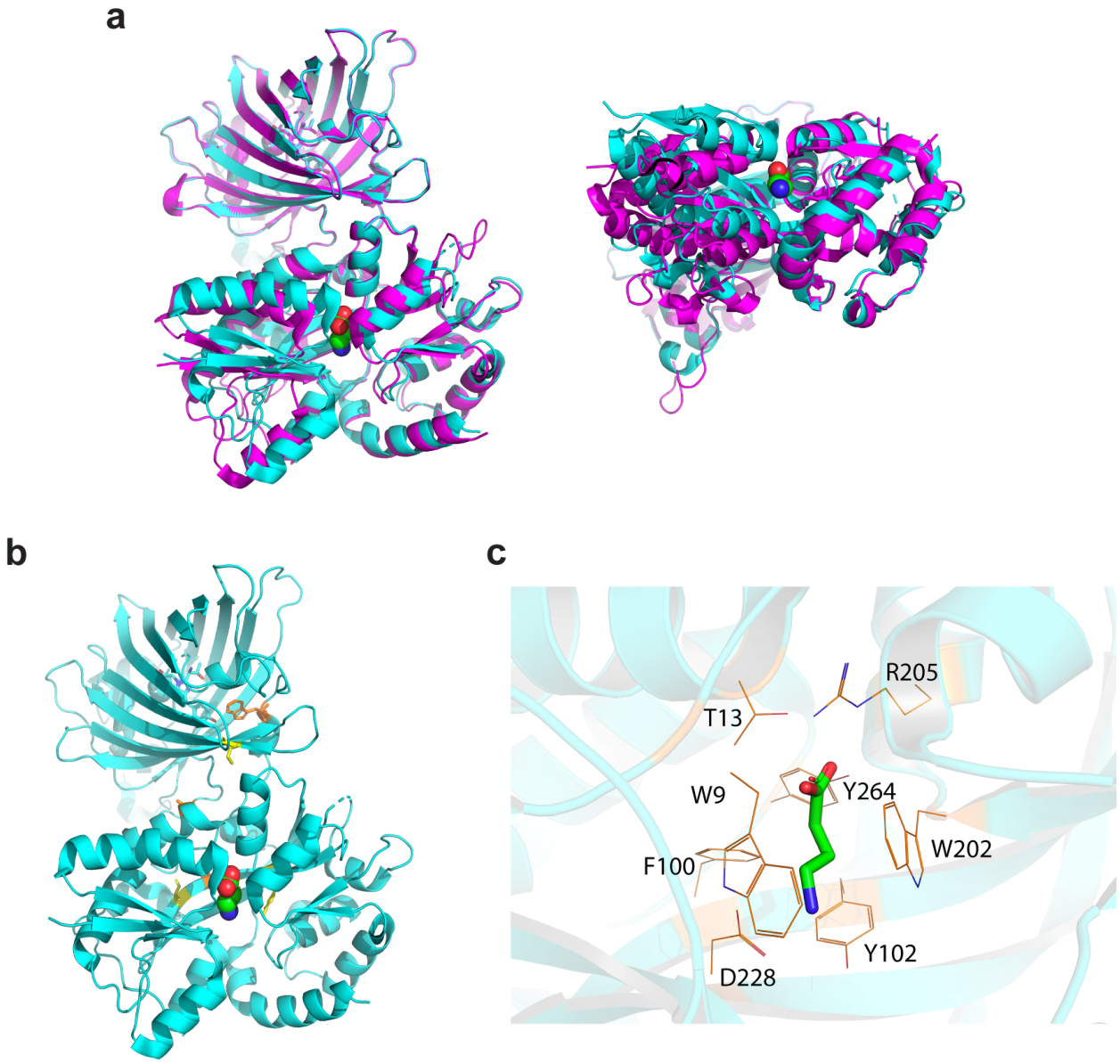

920
921 **Figure 3**

922 **Figure 3 Supplementary Table 1: Data collection and refinement statistics of iGABASnFR2**
923 **in complex with GABA.**

	iGABASnFR2+GABA
Data collection	
Space group	P1 2_1 1
Cell dimensions	
a, *b*, *c* (Å)	76.5, 109.9, 214.3
α, β, γ (°)	90.00, 100.3, 90.00
Resolution (Å)	48.74-2.60 (2.64-2.60)
R_{merge}	0.067 (0.434)
Mean ((I)/sd(I))	11.0 (2.6)
Completeness %	98.5 (99.9)
Multiplicity	3.6 (3.8)
Refinement	
Resolution	47.39-2.60
No. reflections all/free	105768/5396
R_{work}/R_{free}	0.249/0.206
No. atoms	
Protein	24386
Ligand	174
Water	32
B-factor (Å)	
Protein	50.64
Ligand	41.32
Water	35.23
R.M.S. deviations	
Bond lengths (Å)	0.007
Bond angles (°)	1.610

924

925 **Figure 4. Biophysical properties of iGABASnFR variants.**

926 **a.** GABA titrations with purified iGABASnFR protein. Lines indicate fits to mean of n = 5 titration
927 series, error bars are s.e.m.

928 **b.** GABA titrations with sensors expressed on the surface of cultured neurons. Fits (bottom panel)
929 show ΔF/F0 response to increasing concentrations of GABA measured with ROIs placed on
930 individual cell bodies (top panel). In these conditions iGABASnFR2 shows a greater dynamic
931 range than iGABASnFR1, in contrast to results with purified protein. Color lookup table is the
932 same for all images. Scale bar: 50 μm. Illumination: 5.6 mW/mm^2, imaging at 1 frame per sec.

933 **c.** Observed reaction rate constant (K_{obs}) values from stopped-flow measurements for the three
934 sensors.

935 **d.** Stopped flow kinetics of iGABASnFR variants. Lines indicate fits to mean of n = 3 replicates
936 from three separate batches of purified protein.

937 **e.** One-photon excitation and emission spectra of soluble iGABASnFR protein in the presence
938 (10 mM) and absence of GABA.

939 **f.** Two-photon excitation spectra and the computed ΔF/F0 of iGABASnFR variants in the presence
940 (10 mM) and absence of GABA.

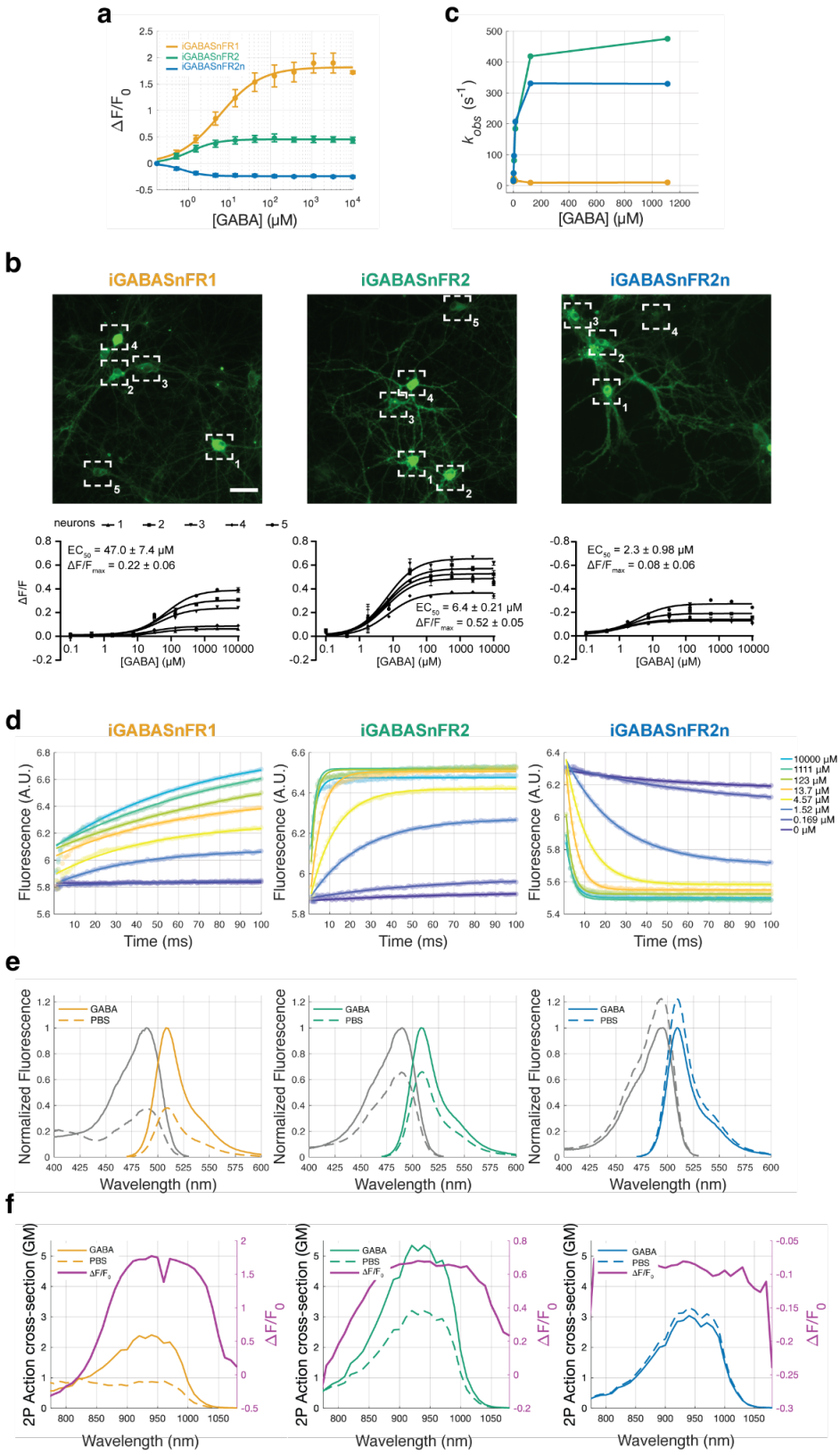

941

942 **Figure 4**

Figure 4 - figure supplement 1. Responses of iGABASnFR variants to GABA-related compounds.

Different iGABASnFR variants (200 nM) were titrated with various concentrations of ligands of interest. Estimated EC_{50} values shown in insets. Each titration has a minimum of n=3 replicates.

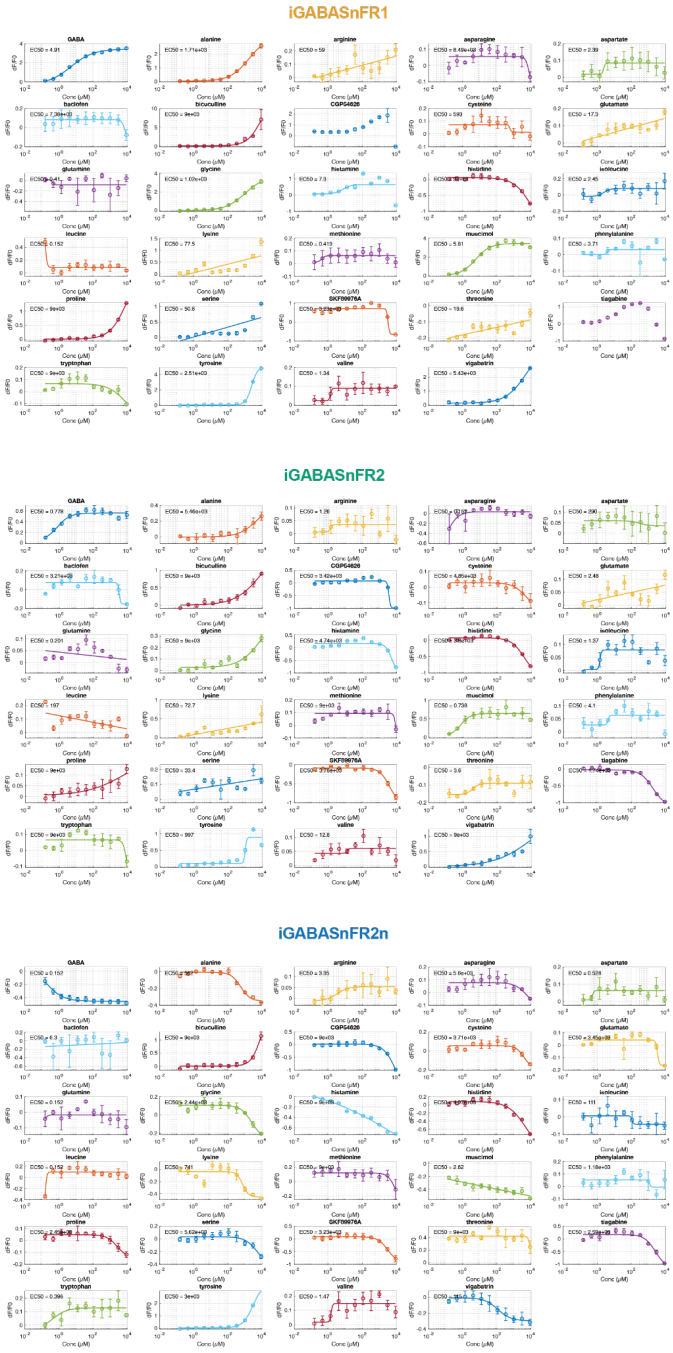

Figure 4 - figure supplement 1

Figure 4 - figure supplement 2. Competition of GABA-related compounds for binding to iGABASnFR variants.

Different iGABASnFR variants (200 nM) were titrated with increasing concentrations of GABA in the presence of different potential competing compounds at 1 mM. Lines indicate fits to mean of n = 3 titration series, error bars are s.e.m. Estimated EC_{50} values shown in insets.

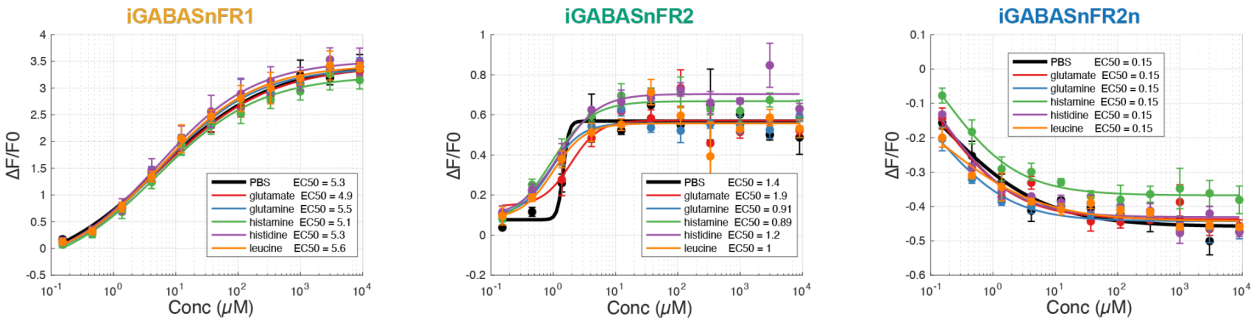

Figure 4 - figure supplement 2

Figure 4 - figure supplement 3. pH titrations of iGABASnFR variants.
Fluorescence response of the three iGABASnFR variants across a pH titration, under GABA-saturated (10 mM, solid lines) and GABA-free (dashed lines) conditions. Fluorescence values are normalized to the peak fluorescence of the GABA-saturated form of each sensor. Measurements were performed using 200 nM sensor concentration. Data points represent the mean of n = 3 technical replicates; error bars indicate s.e.m.

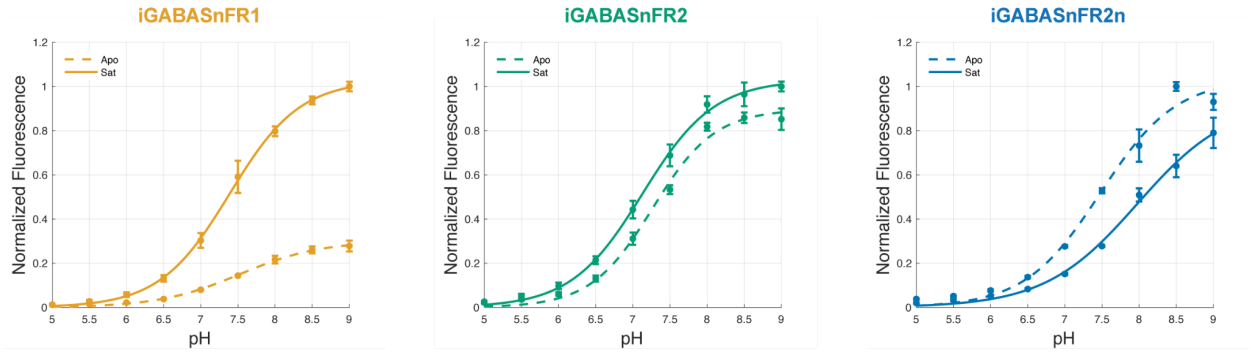

Figure 4 - figure supplement 3

970 **Figure 5. iGABASnFR2 reliably reports direction selectivity in the retina**

971 **a.** Schematic illustration of centrifugal direction selectivity in starburst cell's motion responses.

972 **b.** Spatially asymmetric inhibitory connections (red dots) between starburst cells (SACs) and
973 direction-
974 selective ganglion cells (DSGCs), which are proposed to generate direction selectivity in DSGCs.

975 **c.** Example field of view of SAC processes expressing iGABASnFR1. Yellow region of interest
976 (ROI) is analyzed to evaluate responses to visual stimuli.

977 **d**. Responses to static flash from ROI in **c** but with SACs expressing iGABASnFR2.

978 **e**. Responses to motion stimulus.

979 **f-h**. Results of imaging using iGABASnFR2.

980 **i**. Histograms of response amplitude index (left) and response reliability (right) from SACs
981 expressing iGABASnFR. n = 147 ROIs collected across 5 retinae.

982 **j**. As in **i** but with SACs expressing iGABASnFR2. n = 346 ROIs collected from 3 retinae.
983 Responses to motion stimulus.

984 **k**. Average signals during preferred direction motion with iGABASnFR1 (top, gray) and
985 iGABASnFR2 (bottom, cyan). Line and shading indicate mean ± s.d (n = 147 for iGABASnFR, n
986 = 346 for iGABASnFR2).

987 **l**. Comparison of SNR of the motion response detected with the two sensor versions. p = 0. Two-
988 tailed Mann-Whitney-Wilcoxon test.

989 **m.** Comparison of direction selectivity (CV, circular variance) for the two sensor versions. p =
990 7.812×10^{-6}. Two-tailed Mann-Whitney-Wilcoxon test.

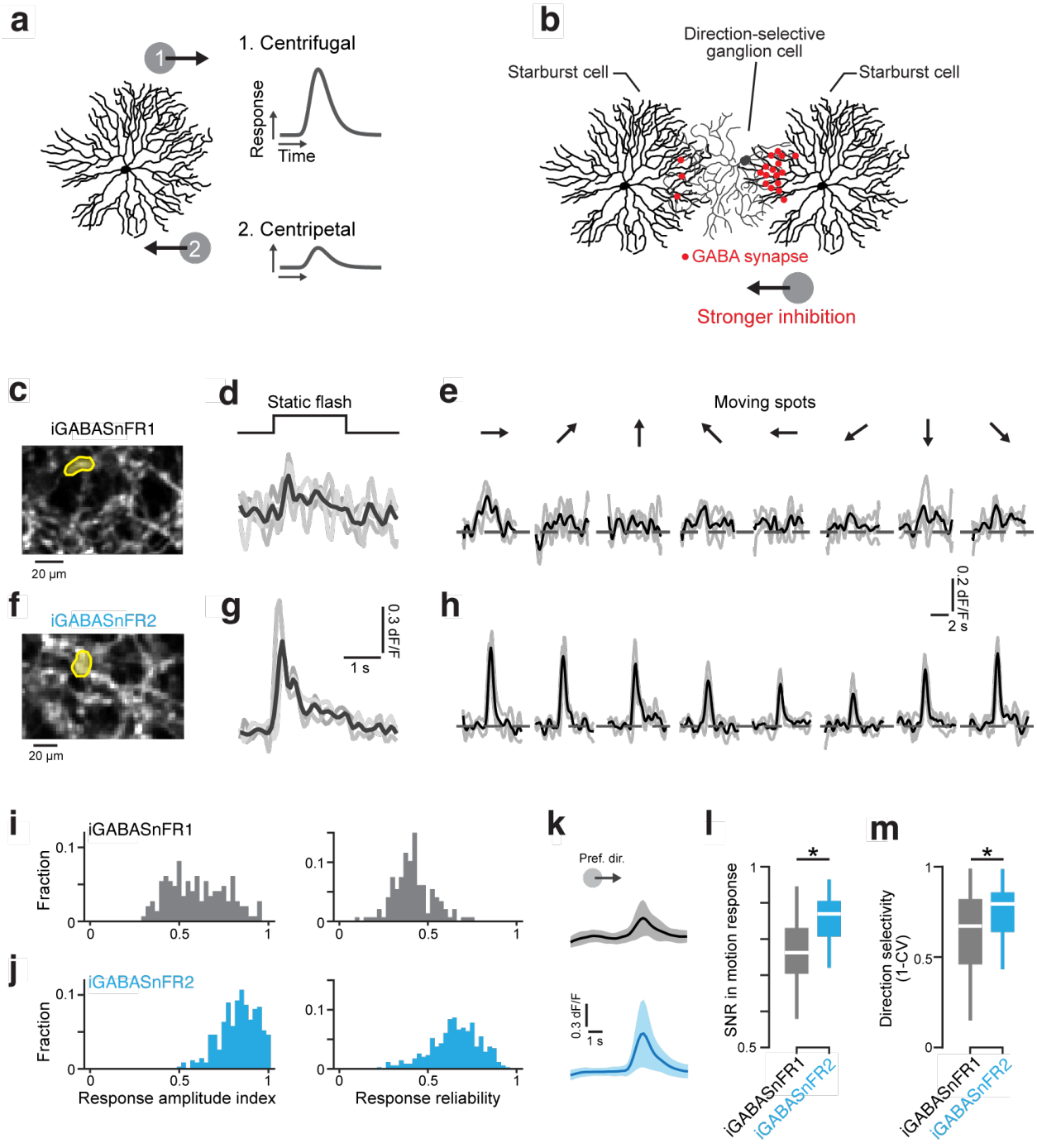
a
1. Centrifugal
Response
Time
2. Centripetal
b
Direction-selective ganglion cell
Starburst cell
Starburst cell
GABA synapse
Stronger inhibition
c
iGABASnFR1
20 µm
d
Static flash
e
Moving spots
f
iGABASnFR2
20 µm
g
0.3 dF/F
1 s
h
0.2 dF/F
2 s
i
iGABASnFR1
Fraction
j
iGABASnFR2
Fraction
Response amplitude index
Response reliability
k
Pref. dir.
0.3 dF/F
1 s
l
SNR in motion response
iGABASnFR1
iGABASnFR2
m
Direction selectivity (1-CV)
iGABASnFR1
iGABASnFR2

Figure 5

Figure 6. iGABASnFR2 Reliably Detects Synaptic GABA Release in Slices and Sensory-Evoked GABA In Vivo

a. *Top*: Image from a whole-cell recording of an iGABASnFR1-expressing hippocampal interneuron in area CA3 of an acute brain slice. To identify axonal boutons, morphology was visualized using Alexa Fluor 594 (red channel), included in the internal solution. The image shown is from the red channel. The axonal segment (dotted rectangle) is shown magnified in the inset, with the position of a schematized 1.5 µm-wide Tornado scan path indicated. Image is the average projection of a z-stack covering 50 µm.

Bottom: iGABASnFR1 fluorescence signal acquired using a 0.5 kHz Tornado scan at the bouton shown above. Horizontal axis: time (700 ms scan duration); vertical axis: spiral turn angle. Trace shows mean $\Delta F/F_0$ response (±SEM) across 15 trials of five action potentials at 50 Hz (arrows).

b. *Top*: As in (**a**), except the image shows iGABASnFR2 fluorescence from an interneuron in area CA1 in an organotypic slice. The image is the average projection of a 30 µm z-stack.

Bottom: As in (**a**), but showing iGABASnFR2 signal from the Tornado scan. Trace shows the mean $\Delta F/F_0$ response (±SEM) across 11 trials of four action potentials delivered at 20 Hz (arrows).

c. Brief rhythmic whisker stimulus triggers volume-transmitted extracellular elevations of GABA in the barrel cortex detected by iGABASnFR2 fluorescence.

Left: Schematic of experimental arrangement, with whisker stimulation via 4 air-puffs at 20 Hz while imaging the contralateral barrel cortex.

Right: Image panel shows barrel cortex area (~300 µm depth) and position of a 1 kHz Tornado-scan. Trace is the single-trial fluorescence response of iGABASnFR2 to a contralateral 200 ms whisker stimulation, as indicated.

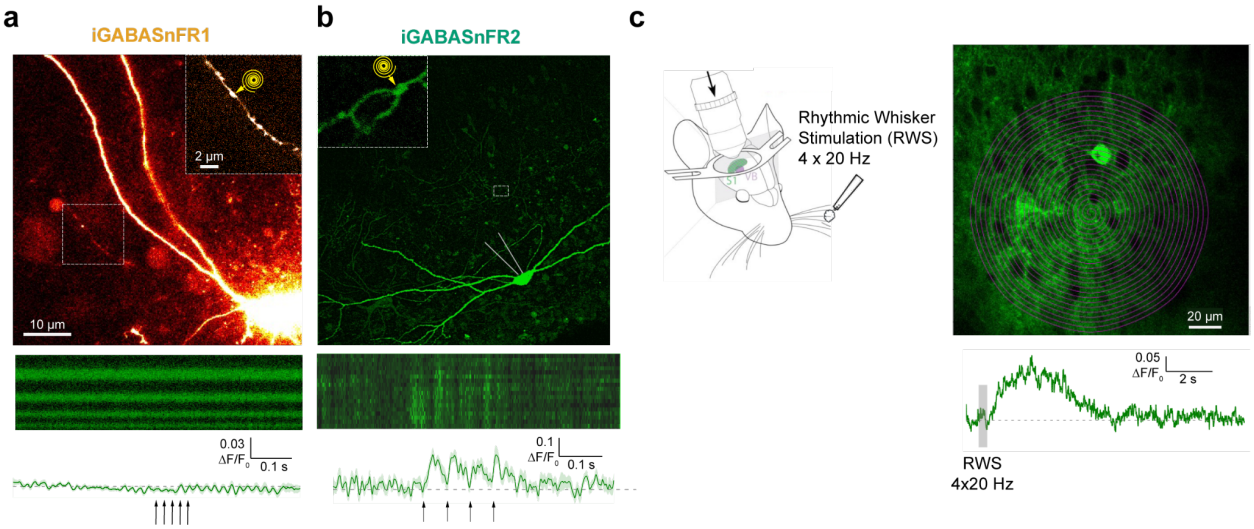

Figure 6

1018 **Supplementary movie 1. iGABASnFR2 detects volume-transmitted GABA signals evoked**
1019 **by sensory stimulation in vivo in the barrel cortex.**

1020 Fluorescence ($\Delta F = F - F_0$) signal from iGABASnFR2 imaged in vivo from a 200 × 30 μm
1021 region of barrel cortex (~150 μm depth). A brief whisker stimulus (4 pulses at 20 Hz; red
1022 dot indicates onset) triggered a macroscopic extracellular GABA elevation. Data were
1023 acquired at 1 kHz using resonant scanning and displayed with a 250 ms sliding average
1024 to suppress heartbeat-related noise.

1025 **Table 1: Photophysical properties of iGABASnFR variants as purified proteins**

1026

	λ_{abs} (nm)	λ_{Ex} (nm)	λ_{Em} (nm)	ΔF/F	ε (M/cm^2)		Φ		τ (ns)	
					GABA	**PBS**	**GABA**	**PBS**	**GABA**	**PBS**
iGABASnFR1	490	489	508	1.9	14070 ± 600	5375 ± 220	0.58 ± 0.01	0.54 ± 0.03	2.22 ± 0.05	2.32 ± 0.01
iGABASnFR2	490	490	508	0.46	26195 ± 390	19800 ± 380	0.61 ± 0.02	0.54 ± 0.01	2.29 ± 0.08	2.30 ± 0.02
iGABASnFR2n	493	496	509	-0.13	12390 ± 690	13000 ± 220	0.72 ± 0.02	0.76 ± 0.01	2.71 ± 0.02	2.72 ± 0.02

1027